

Extended $H\alpha$ over compact far-infrared continuum in dusty submillimeter galaxies

Insights into dust distributions and star-formation rates at $z \sim 2$

Chian-Chou Chen (陳建州)^{1,2}, C. M. Harrison^{3,1}, I. Smail⁴, A. M. Swinbank⁴, O. J. Turner⁵, J. L. Wardlow⁶, W. N. Brandt^{7,8,9}, G. Calistro Rivera^{10,1}, S. C. Chapman^{11,12,13,14}, E. A. Cooke⁴, H. Dannerbauer^{15,16}, J. S. Dunlop⁵, D. Farrah^{17,18}, M. J. Michałowski¹⁹, E. Schinnerer²⁰, J. M. Simpson², A. P. Thomson²¹, and P. P. van der Werf¹⁰

¹ European Southern Observatory, Karl Schwarzschild Strasse 2, Garching, Germany

² Academia Sinica Institute of Astronomy and Astrophysics, PO Box 23-141, Taipei 10617, Taiwan
e-mail: ccchen@asiaa.sinica.edu.tw

³ School of Mathematics, Statistics and Physics, Newcastle University, Newcastle upon Tyne NE1 7RU, UK

⁴ Centre for Extragalactic Astronomy, Department of Physics, Durham University, South Road, Durham DH1 3LE, UK

⁵ Institute for Astronomy, University of Edinburgh, Royal Observatory, Blackford Hill, Edinburgh EH9 3HJ, UK

⁶ Physics Department, Lancaster University, Lancaster LA14YB, UK

⁷ Department of Astronomy & Astrophysics, 525 Davey Lab, The Pennsylvania State University, University Park, PA 16802, USA

⁸ Institute for Gravitation and the Cosmos, The Pennsylvania State University, University Park, PA 16802, USA

⁹ Department of Physics, The Pennsylvania State University, University Park, PA 16802, USA

¹⁰ Leiden Observatory, Leiden University, PO Box 9513, 2300 Leiden, The Netherlands

¹¹ Department of Physics & Astronomy, University of Victoria, BC V8X 4M6 Victoria, Canada

¹² Department of Physics and Atmospheric Science, Dalhousie University, Halifax, NS B3H 4R2, Canada

¹³ NRC Herzberg Astronomy and Astrophysics, 5071 West Saanich Road, Victoria BC V9E 2E7, Canada

¹⁴ Department of Physics and Astronomy, University of British Columbia, Vancouver, BC V6T 1Z1, Canada

¹⁵ Instituto de Astrofísica de Canarias (IAC), 38205 La Laguna, Tenerife, Spain

¹⁶ Universidad de La Laguna, Dpto. Astrofísica, 38206 La Laguna, Tenerife, Spain

¹⁷ Department of Physics and Astronomy, University of Hawaii, 2505 Correa Road, Honolulu, HI 96822, USA

¹⁸ Institute for Astronomy, 2680 Woodlawn Drive, University of Hawaii, Honolulu, HI 96822, USA

¹⁹ Astronomical Observatory Institute, Faculty of Physics, Adam Mickiewicz University, ul. Słoneczna 36, 60-286 Poznań, Poland

²⁰ Max – Planck Institut für Astronomie, Königstuhl 17, 69117 Heidelberg, Germany

²¹ The University of Manchester, Oxford Road, Manchester M139PL, UK

Received 10 July 2019 / Accepted 5 February 2020

ABSTRACT

By using data from the Atacama Large Millimeter/submillimeter Array and near-infrared (NIR) integral field spectrographs, including both Spectrograph for INtegral Field Observations in the Near Infrared and K -band Multi Object Spectrograph on the Very Large Telescope, we investigate the two-dimensional distributions of $H\alpha$ and rest-frame far-infrared (FIR) continuum in six submillimeter galaxies (SMGs) at $z \sim 2$. At a similar spatial resolution (~ 0.5 FWHM; ~ 4.5 kpc at $z = 2$), we find that the half-light radius of $H\alpha$ is significantly larger than that of the FIR continuum in half of the sample, and on average $H\alpha$ is a median factor of 2.0 ± 0.4 larger. Having explored various ways to correct for the attenuation, we find that the attenuation-corrected $H\alpha$ -based star-formation rates (SFRs) are systematically lower than the infrared (IR)-based SFRs by at least a median factor of 3 ± 1 , which cannot be explained by the difference in half-light radius alone. In addition, we find that in 40% of cases the total V -band attenuation (A_V) derived from energy balance modeling of the full ultraviolet (UV)-to-FIR spectral energy distributions (SEDs) is significantly higher than what is derived from SED modeling using only the UV-to-NIR part of the SEDs, and the discrepancy appears to increase with increasing total infrared luminosity. Finally, in considering all of our findings along with the studies in the literature, we postulate that the dust distributions in SMGs, and possibly also in less IR luminous $z \sim 2$ massive star-forming galaxies, can be decomposed into the following three main components: the diffuse dust heated by older stellar populations, the more obscured and extended young star-forming H II regions, and the heavily obscured central regions that have a low filling factor but dominate the infrared luminosity in which the majority of attenuation cannot be probed via UV-to-NIR emissions.

Key words. galaxies: formation – galaxies: ISM – galaxies: high-redshift – galaxies: structure – galaxies: star formation – submillimeter: galaxies

1. Introduction

Measurements of the star-formation rate (SFR) across cosmic time provide one of the most fundamental constraints to

models of galaxy formation and evolution (e.g., Somerville & Davé 2015). Comparisons between the SFR and other galaxy properties have yielded essential insights into the physics of galaxy assembly, such as the Schmidt–Kennicutt relationship

(Schmidt 1959; Kennicutt 1989) and the so-called galaxy star-forming main sequence (e.g., Noeske et al. 2007; Elbaz et al. 2011; Whitaker et al. 2012; Schreiber et al. 2015).

The vital role that SFR measurements play in constraining galaxy models means that the calibrations and diagnostics for various tracers have been extensively studied (Kennicutt & Evans 2012). Thanks to technical advances in both ground-based telescopes and space-based satellites, SFRs can be estimated through a wide spectral range of emission from X-ray to radio, using both continuum and line emission (e.g., Ranalli et al. 2003; Lehmer et al. 2010; Murphy et al. 2011). As measurements made at different wavelengths are sensitive to different ages of the stellar populations (Calzetti 2013) and since they are affected by dust attenuation to a different level, in principle, SFR tracers at different wavelengths should all be considered and exploited for their complementary strengths in diagnostics. Indeed in the local Universe, calibrations have been derived to obtain the total SFRs and, in particular, to address dust attenuation by combing ultraviolet (UV), $H\alpha$, and infrared data (Hao et al. 2011). This has been done both locally for individual star-forming regions (Calzetti et al. 2007; Li et al. 2013) and globally for entire galaxies (Kennicutt et al. 2009; Catalán-Torrecilla et al. 2015; Brown et al. 2017).

Beyond the nearby universe, the volume-averaged SFR density rises rapidly by over an order of magnitude of $z \sim 2$ (Madau & Dickinson 2014). During these times, the SFR density is dominated by infrared bright galaxies (Le Flocc'h et al. 2005; Smolčić et al. 2009; Gruppioni et al. 2013; Swinbank et al. 2014), which are classified as (ultra)luminous infrared galaxies ((U)LIRGs; Sanders & Mirabel 1996) with a total infrared luminosity greater than $(10^{12})10^{11} L_{\odot}$. This means that at $z \sim 2$, the infrared component of the SFRs becomes dominant, and the correction of dust attenuation becomes critical for galaxy samples in which the SFRs are predominantly measured via the UV and optical. Indeed, continuum and emission lines in the UV and optical are used extensively at high redshifts to measure SFRs given their accessibility and technical advances, and the cosmic SFR density has been estimated with this method up to $z \sim 10$ (e.g., Reddy & Steidel 2009; Bouwens et al. 2011; Ellis et al. 2013; Oesch et al. 2015; McLeod et al. 2016; Ishigaki et al. 2018).

However, the method to correct for dust attenuation for UV and optical measurements at high redshifts is currently a topic of debate. For example, the common method to correct the UV SFRs using the correlation between the ratio of infrared and UV luminosity and the spectral slope in the UV, the $IRX-\beta$ relation, is subject to many systematics including turbulence, the age of the stellar populations, and the dust compositions and geometry (e.g., Howell et al. 2010; Casey et al. 2014; Chen et al. 2017; Popping et al. 2017; Narayanan et al. 2018). Similarly, due to the faintness of $H\beta$, the correction for the $H\alpha$ -based SFRs using the Balmer decrement is also not straightforward. To bypass the difficulty of obtaining the Balmer decrement, stellar attenuation derived from spectral energy distributions (SED) fitting based on UV-to-near-infrared (NIR) photometry has been adopted (e.g., Sobral et al. 2013). However, the relation between the nebular attenuation and the stellar attenuation has not been well determined, either locally (e.g., Kreckel et al. 2013) or at high redshifts (e.g., Calzetti et al. 2000; Wild et al. 2011; Kashino et al. 2013; Price et al. 2014; Reddy et al. 2015; Puglisi et al. 2016; Theios et al. 2019).

Regardless of whether the galaxies are located in the nearby universe or at high redshifts, one of the main issues that is faced when correcting dust attenuation has been the spatial distribution of dust. It is assumed that dust acts as a foreground screen

and spatially coincides with the underlying emissions, which is partly motivated by the findings in the local spiral galaxies (e.g., Kennicutt et al. 2009; Bendo et al. 2012). In addition, as a result of how different attenuations are oftentimes found in nebular emission lines, such as $H\alpha$ compared to the stellar continuum (e.g., Calzetti et al. 2000), the dust distribution is normally perceived to have the following two main components: the diffuse dust in the interstellar medium (ISM) that obscured older stellar populations and the dustier component obscuring the H II regions (e.g., Wild et al. 2011; Price et al. 2014; Reddy et al. 2015; Leslie et al. 2018). This two-component dust distribution model is one of the major assumptions that goes into the SED modeling that employs the energy balance technique, such as MAGPHYS (da Cunha et al. 2008, 2015) and CIGALE (Noll et al. 2009).

In more chaotic and gas-rich environments, in particular at $z \sim 2$, there is increasing evidence suggesting that the aforementioned assumptions may need to be adjusted. For example, studies using the Atacama Large Millimeter/submillimeter Array (ALMA) have found, almost ubiquitously, that the massive dusty galaxies at high redshifts have very compact morphology in far-infrared (FIR) continuum, with a half-light radius of $\sim 1-2$ kpc (e.g., Simpson et al. 2015; Ikarashi et al. 2015, 2017; Barro et al. 2016; Harrison et al. 2016; Hodge et al. 2016, 2019; Spilker et al. 2016; Tadaki et al. 2017a; Oteo et al. 2017; Fujimoto et al. 2018). In addition, many other tracers of star-forming regions are found to be spatially offset from, or much larger than, the FIR continuum, including the stellar continuum in the UV and optical (e.g., Chen et al. 2015; Hodge et al. 2016; Cowie et al. 2018; Gómez-Guijarro et al. 2018), radio continuum at 1.4 and 3 GHz (e.g., Biggs & Ivison 2008; Miettinen et al. 2017; Thomson et al. 2019), and emission lines, such as [CII] (Gullberg et al. 2018; Litke et al. 2019), ^{12}CO (Spilker et al. 2015; Chen et al. 2017; Tadaki et al. 2017b; Calistro Rivera et al. 2018; Dong et al. 2019), H_2O (Apostolovski et al. 2019), and $H\alpha$ (Alaghband-Zadeh et al. 2012; Menéndez-Delmestre et al. 2013; Chen et al. 2017; Nelson et al. 2019). While these studies mostly focus on more infrared (IR) luminous sources, these results suggest that the dust distribution at $z \sim 2$ could be significantly different than in galaxies in the nearby universe, and spatially resolved studies comparing various star-formation tracers are needed in order to better understand the physics of star formation during the epoch when most of the massive elliptical galaxies seen in the nearby universe formed (e.g., Lilly et al. 1999; Hickox et al. 2012; Toft et al. 2014; Simpson et al. 2014; Chen et al. 2016; Wilkinson et al. 2017).

This paper is partly motivated by the work of Chen et al. (2017) in which we found that in a submillimeter galaxy (SMG), ALESS67.1, at $z = 2.12$ where we managed to gather subarc-second UV-to-NIR continuum, FIR continuum, ^{12}CO , and $H\alpha$, the size of FIR continuum is a factor of $\sim 4-6$ smaller than that of all of the other emissions. Calistro Rivera et al. (2018) have extended the size comparison between FIR continuum and ^{12}CO to a sample of four SMGs, finding that $^{12}\text{CO}(J = 3-2)$ is larger than the FIR continuum by a factor > 2 . They propose that the size difference can be explained by temperature and optical depth gradients alone. In this paper we aim to extend the comparison between the FIR continuum and $H\alpha$ to a larger sample of SMGs. In Sect. 2 we provide details about our sample selection and data. The analyses and measurements are presented in Sect. 3. We discuss the implications of our findings in Sect. 4 and the summary is given in Sect. 5. Throughout this paper, we define the size to be the half-light radius. We assume the *Planck* cosmology: $H_0 = 67.8 \text{ km s}^{-1} \text{ Mpc}^{-1}$, $\Omega_M = 0.31$, and $\Omega_{\Lambda} = 0.69$ (Planck Collaboration XVI 2014).

Table 1. General information about the sample and the data

ID	RA _{ALMA} [J2000]	Dec _{ALMA} [J2000]	AGN ^(a)	PSF _{ALMA,nat} [arcsec]	PSF _{ALMA,tap} [arcsec]	IFU	IFU _{band}	PSF _{IFU} [arcsec]
ALESS17.1	53.030410	-27.855765	X-ray	0.17 × 0.15	0.66 × 0.62	SINFONI	<i>H</i>	0.65
ALESS66.1	53.383053	-27.902645	No	0.17 × 0.13	0.47 × 0.45	SINFONI	<i>K</i>	0.48
ALESS67.1	53.179981	-27.920649	X-ray	0.18 × 0.15	0.66 × 0.62	SINFONI	<i>HK</i>	0.66
ALESS75.1	52.863303	-27.930928	IR	0.17 × 0.12	0.57 × 0.54	SINFONI	<i>HK</i>	0.56
AS2UDS292.0	34.322638	-5.2300513	X-ray	0.22 × 0.19	0.46 × 0.42	KMOS	<i>K</i>	0.46
AS2UDS412.0	34.422392	-5.1810288	No	0.25 × 0.23	0.56 × 0.52	KMOS	<i>K</i>	0.55

Notes. ^(a)The AGN classification in the X-ray is based on catalog matching; ALESS SMGs are matched to the *Chandra* 7 Ms catalog and classified as AGN based on the criteria set in Luo et al. (2017). The AS2UDS SMGs are matched to the *Chandra* X-UDS catalog (Kocevski et al. 2018) with a simple luminosity cut of $L_{2-10\text{keV}} > 3 \times 10^{42} \text{ erg s}^{-1}$, which is one of the criteria used in Luo et al. (2017). The steep slope in mid-infrared has suggested that ALESS75.1 is an IR AGN (Simpson et al. 2014; Stanley et al. 2018).

2. Sample, data, and reductions

2.1. Sample

Our sample of six SMGs was drawn from two parent SMG samples. One is the ALESS sample (Hodge et al. 2013; Karim et al. 2013), which was obtained from a Cycle 0 ALMA 850 μm follow-up survey targeting a flux-limited sample of 126 submillimeter sources detected by a LABOCA (Siringo et al. 2009) 870 μm survey in the Extended *Chandra* Deep Field South (ECDFS) field (LESS survey; Weiß et al. 2009). These sources were subsequently observed at a higher angular resolution with ALMA (Hodge et al. 2016, 2019). The other is the AS2UDS sample (Simpson et al. 2017; Stach et al. 2018, 2019), which is based on a Cycle 1,3,4,5 ALMA 850 μm follow-up program of all 716 $> 4\sigma$ submillimeter sources that were uncovered by the SCUBA-2 850 μm legacy survey in the UKIDSS-UDS field (Geach et al. 2017).

To compare the morphology of FIR continuum and H α and, in particular, the measurement of sizes, spatially resolved observations are required. In regards to SMGs, this typically means that observations are taken at $\lesssim 0''.5$ (e.g., Simpson et al. 2015; Alaghband-Zadeh et al. 2012). Therefore, for the selection of galaxies from ALESS and AS2UDS for this study, firstly, we require that targets have $\lesssim 0''.5$ angular resolution ALMA band 7 continuum imaging, which has a matched or better spatial resolution than the seeing-limited H α data so it allows for direct comparisons in spatial distributions between cold dust continuum and H α . The majority of the AS2UDS SMGs satisfy this criterion (Stach et al. 2019) and for ALESS SMGs we consider the ones published in Hodge et al. (2016) and an extra sample obtained through the program 2016.1.00735.S (PI: C. M. Harrison).

The second step is based on the positions of these SMGs to search the Very Large Telescope (VLT) archive for the existing integral field unit (IFU) (Spectrograph for INtegral Field Observations in the Near Infrared; SINFONI or *K*-band Multi Object Spectrograph; KMOS) observations. We reduced the archival data following the methods described in the next section. To allow creations of two-dimensional (2D) intensity maps, we kept the SMGs that have a high signal-to-noise ratio (S/N) H α detection, which correspond to a typical flux density of $\sim 10^{-16} \text{ erg s}^{-1} \text{ cm}^{-2}$; however, we removed obvious broad line active galactic nuclei (AGN, BLAGN). While the archival data have been taken from different programs so it is difficult to assess the potential selection biases, we note that the H α flux density distribution ($5 \times 10^{-17} - 3 \times 10^{-16} \text{ erg s}^{-1} \text{ cm}^{-2}$) from our sam-

ple of SMGs follows what is reported in the literature regarding other SMG samples (Swinbank et al. 2004; Casey et al. 2017). Under these two criteria, we have obtained four ALESS and two AS2UDS SMGs, and their basic properties are given in Table 1.

Based on the SED analyses shown later using the MAGPHYS code, we find that these six SMGs have a median dust mass of $\log(M_{\text{dust}}) = 8.9 M_{\odot}$, a median stellar mass of $\log(M_{*}) = 11.2 M_{\odot}$, and a median SFR of $\log(\text{SFR}) = 2.4 M_{\odot} \text{ yr}^{-1}$. This means that on average, they are located in the upper part of the massive end of the SFR- M_{*} main sequence at $z \sim 2$, which is consistent with the behavior of the general SMG population (da Cunha et al. 2015).

2.2. SINFONI and KMOS IFU

The SINFONI-IFU data were taken for the four ALESS sources between October 2013 and December 2014 under the program IDs 091.B-0920 and 094.B-0798. We used the *H*-, *K*-, and *HK*-band to observe ALESS17.1, ALESS66.1, and both ALESS67.1 and ALESS75.1, respectively, covering the [N II]/H α lines in all four sources and the [O III]/H β lines in the last two. The spectral resolution is $R > 1500$, which is sufficient to separate H α and the two [N II] lines. The data were reduced using the ESOREX (ESO Recipe Execution Tool; Freudling et al. 2013) pipeline, and additional custom routines were applied to improve the sky subtraction. Solutions for flux calibration were derived using the IRAF routines STANDARD, SENSFUNC, and CALIBRATE on the standard stars, which normally were observed within two hours of the science observations and processed along with the scientific data. Standard stars were also used to produce the point spread functions (PSFs)¹, which were fit with 2D Gaussian models to derive the angular resolution.

The *K*-band KMOS data on AS2UDS SMGs were taken by the KMOS^{3D} survey (Wisnioski et al. 2015) under the program IDs 093.A-0079 and 096.A-0025. The data reduction primarily made use of SPARK (Software Package for Astronomical Reduction with KMOS; Davies et al. 2013), which was implemented using the ESOREX. In addition to the SPARK recipes, custom PYTHON scripts were run at different stages of the pipeline and are described in detail in Turner et al. (2017). Standard star observations were carried out on the same night as the science observations and were processed in an identical

¹ The ideal way to monitor the PSF for SINFONI is to request the PSF standard observations, but they do not exist for any of the data sets we used. However, we checked the recorded seeing conditions between the standard stars and the science targets and we find that they agree to $\sim 15\%$ without a significant systematic offset.

manner to the scientific data, which were used for flux calibration and PSF generation. Sky subtraction was enhanced using the SKYTWEAK option within SPARK (Davies 2007), which counters the varying amplitude of OH lines between exposures by scaling families of OH lines independently to match the data.

The astrometry of both the SINFONI and the KMOS data was corrected by aligning the continuum of the IFU cube to the corresponding ground-based imaging, including TENIS *K*-band (Hsieh et al. 2012) or MUSYC *H*-band in CDF-S (Taylor et al. 2009), and UKIDSS *K*-band (Lawrence et al. 2007) in UDS, which was first aligned to the *Gaia* DR2 catalog (Gaia Collaboration 2018) based on sources with $R = 15\text{--}20$ mag (in AB). By doing so, we found a significant systematic shift to the north in declination of the ground-based imaging in CDF-S with respect to the *Gaia* sources by $\sim 0''.3 \pm 0''.1$, which is consistent with similar findings in the literature (e.g., Xue et al. 2011; Dunlop et al. 2017; Luo et al. 2017; Scholtz et al. 2018). No systematic offset is found in UDS imaging. Assuming the ALMA astrometry aligns with *Gaia* DR2, the precision of astrometry of the IFU data derived through this exercise is $< 0''.2$ (around one pixel of the IFU data).

2.3. ALMA 870 μm continuum

The ALMA data of ALESS17.1, ALESS67.1, and the two AS2UDS SMGs have been published and described in detail in Hodge et al. (2016), Chen et al. (2017), and Stach et al. (2018). To present the data self-consistently, we reanalyzed the data by first creating the calibrated measurement set using the pipeline reduction scripts provided by the ALMA archive, with a corresponding CASA version used to generate the scripts. ALESS66.1 and ALESS75.1 were observed in Cycle 4 as a comparison sample in order to test the size difference between SMGs with or without detectable active galactic nuclei (AGN; Project ID: 2016.1.00735.S). We again used the pipeline reduction script to create the calibrated measurement set under CASA version 4.7.2. All ALMA data were tuned to the default band 7 continuum observations, which are centered at 344 GHz/870 μm , with 4×128 dual polarization channels over the 8 GHz bandwidth. At this frequency, ALMA has a $17''.3$ primary beam in full width half maximum (FWHM).

We then made the following two sets of images: One was created using natural weighting and the other was tapered to a spatial resolution that matched the $\text{H}\alpha$ data. Both sets of images were deconvolved using the CLEAN algorithm, and circular regions with a $1''.5$ radius centered at the SMGs were cleaned down to 2σ . The typical angular resolution under natural weighting is $\sim 0''.2$, and $\sim 0''.5$ for the tapered images (Table 1), also the corresponding depths in root mean square (rms) are $30\text{--}70 \mu\text{Jy beam}^{-1}$ and $60\text{--}300 \mu\text{Jy beam}^{-1}$, respectively.

3. Analyses and measurements

3.1. SINFONI and KMOS IFU

For spectral analyses, we used the code detailed in Chen et al. (2017) to fit both the emission lines and the NIR continuum. In short, the code first performs fits for each spectrum with various models including continuum and different combinations of the $\text{H}\alpha$, [N II], and [S II] lines. It then selects the best model based on the Akaike information criterion and, in particular, the version that is corrected for the finite sample size (AICc; Hurvich & Tsai 1989). Finally, a model fit with line components is considered significant if the fit, compared to a simple continuum-

only model, has a lower AICc and provides a χ^2 improvement of $\Delta\chi^2 > 16^2$ for an $\text{H}\alpha$ -only model and an additional improvement of $\Delta\chi^2 > 9$ for each additional line. The fits are weighted against the sky spectrum provided by Rousselot et al. (2000), and when calculating χ^2 , the wavelength ranges corresponding to the sky-lines are masked. The velocity dispersion is corrected in quadrature for instrumental broadening. The errors are derived using Monte Carlo simulations; in particular, we created fake spectra by injecting the model profile into spectra extracted from randomly selected regions of the data cube with the same circular aperture used for the detection spectrum. The errors are then obtained from the standard deviations between the fit results and the input model.

To measure the total line flux densities, we employed the curve-of-growth analyses in which the integrated line flux densities are measured with the increasing size of circular apertures. The total line flux densities are then obtained at a certain radius beyond which the line flux densities do not significantly increase, thus they hit a plateau. This approach is independent of any 2D surface brightness models and it is also adopted in some recent work in the literature (e.g., Chen et al. 2017; Förster Schreiber et al. 2018). To do such analyses, first the centroid of the circular aperture needs to be determined. We define the centers of $\text{H}\alpha$ curve-of-growth analyses to be the centroids of the ellipses best fit to the isophotes of the 2D emission line maps, specifically the isophotes that have their sizes matched to the corresponding spatial resolution. The 2D emission line maps are created by performing line fitting on spectra extracted from each individual pixels, with an adaptive binning approach up to 5×5 pixels depending on the S/Ns (e.g., Swinbank et al. 2006; Chen et al. 2017). In pixels where the fitting still fails after 5×5 binning to give an adequate S/N, we leave the pixel blank without a fit. The caveat of this approach is that the signals are weighted toward the higher S/N pixels. The 2D emission line maps are shown in Fig. 2, and outcome of the curve-of-growth analyses is plotted in Fig. 1, and the measurements are given in Table 2.

The $\text{H}\alpha$ sizes are measured in two ways. The first way is to measure the sizes in the curve-of-growth analyses, as shown in Fig. 2. We used a spline linear fit with the measurements and derived uncertainties and the radius that that corresponds to half of the normalized flux density. The same procedure was applied on the PSFs; by subtracting the PSF sizes from the measured sizes in quadrature, we derived the deconvolved, intrinsic sizes. We applied the same analyses to both $\text{H}\alpha$ and the 870 μm continuum. The results are given in Table 2.

The second method is to use GALFIT (v3.0.5; Peng et al. 2010) in order to conduct single Sérsic profile fits. The basic procedure closely follows Chen et al. (2015). Before fitting, we first converted the 2D $\text{H}\alpha$ emission line maps to the units in counts, instead of flux density, which is recommended in the GALFIT user manual. The PSF images used for GALFIT are sky-subtracted and properly centered at the peak of the PSFs, and we confirm that all PSFs are Nyquist sampled ($\text{FWHM} > 2$ pixels). We limited the Sérsic index range to between 0.1 and 4 and left the rest of the parameters free without constraints. The results are given in Table 2 and they are consistent with those obtained from the curve-of-growth methods. To check whether our results are dependent on the line fitting code, we also performed the Sérsic fits on the narrow-band $\text{H}\alpha$ imaging, which is produced

² Equivalent to an $S/N > 4\sigma$ assuming Gaussian noise and that the noise is not correlated among wavelength channels.

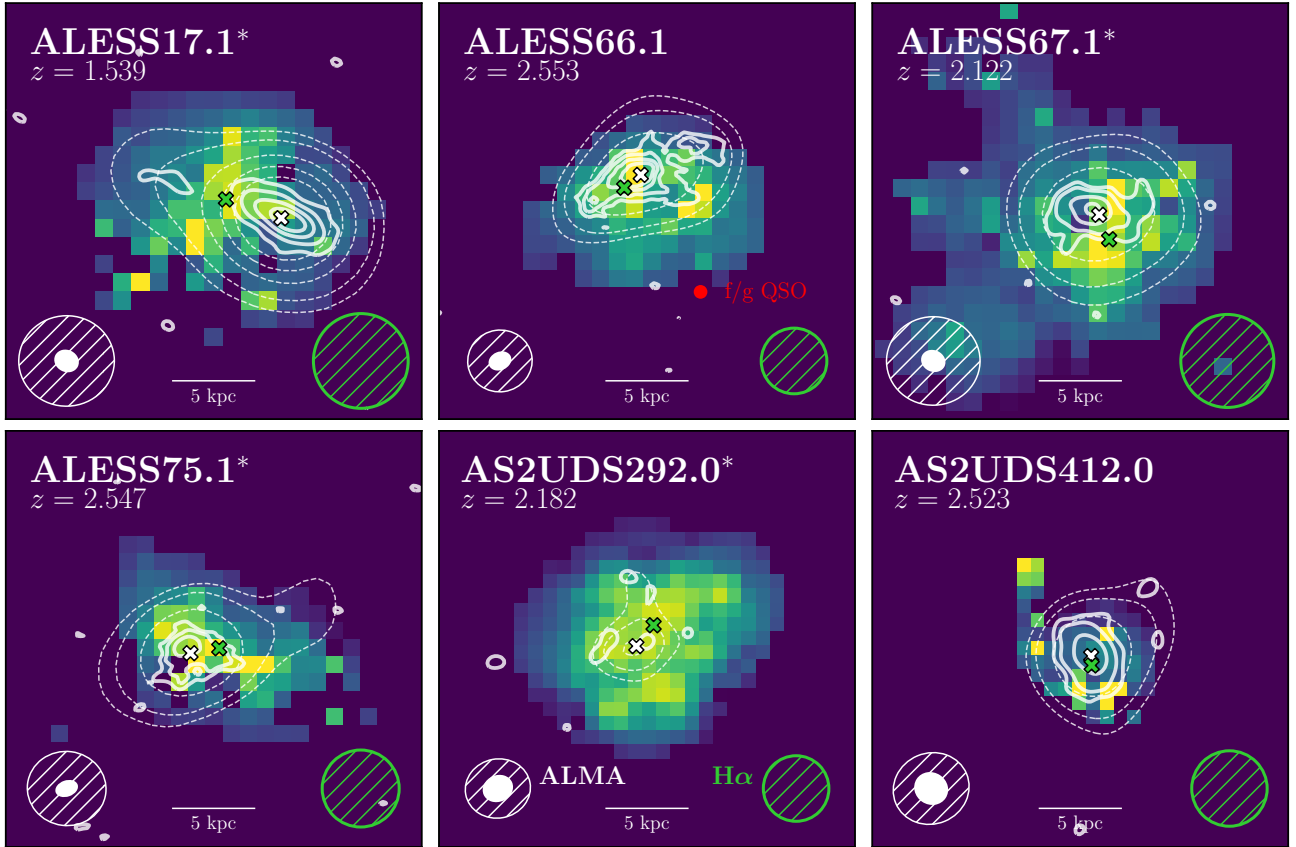


Fig. 1. Two-dimensional H α maps of our sample SMGs (Table 1) with a size of 25×25 kpc and a color stretch from zero to 99.5% of the peak. The solid and the dashed contours starting from 3σ are overlaid on top to show two versions of the ALMA $870 \mu\text{m}$ continuum, respectively; one was produced using natural weighting, resulting in $\sim 0''.2$ resolution, and the other is tapered to $\sim 0''.5$ resolution, matching to the resolution of the H α images. The resolution beams in sizes of FWHM are plotted in the bottom corners and the exact sizes are given in Table 1. White and green crosses mark the positions adopted as the centers of the curve-of-growth analyses, for $870 \mu\text{m}$ continuum and H α , respectively. These positions are centroids of the best-fit ellipses to the isophotes of the corresponding 2D images, with the details described in Sect. 3. Sources that are identified to host an AGN are marked with an asterisk after the ID. The nearby foreground quasar next to ALESS66.1 is marked with a red dot. We find that the rest-frame FIR emissions appear to be smaller in scale than H α in most sources.

by averaging the wavelength channels within the FWHM of the line, and we again find consistent results.

The size of the H α emission has a range of 1–7 kpc from the curve-of-growth method with a median size of $r_{e,\text{H}\alpha,\text{cog}} = 3.9 \pm 0.3$ kpc (bootstrapped uncertainty). This is consistent with the one in the major axis that was obtained from the Sérsic profile fits.

3.2. ALMA $870 \mu\text{m}$ continuum

All six SMGs are significantly detected (peak $S/N > 5$) in both sets (natural weighting and tapered) of the ALMA images (Fig. 1). We measured their $870 \mu\text{m}$ continuum flux densities and sizes in the visibility domain by using the CASA package UVMODELFIT assuming elliptical Gaussian profiles, except for ALESS75.1 in which there is another serendipitous detection in the map (Hodge et al. 2013; ALESS75.2 is $\sim 10''$ away, so it is not visible in Fig. 1) so the package UVMULTIFIT (Martí-Vidal et al. 2014) was used. We attempted to adopt disk models³ in the fitting, but Gaussian models produce better fits with lower χ^2 in all cases. The results are given in Table 2 along with those derived from the curve-of-growth analyses.

³ The disk model in CASA is not an exponential disk but a uniformly bright disk.

The median size derived from the one-dimensional (1D) curve-of-growth method ($r_{e,870,\text{cog}}$) is 1.9 ± 0.2 kpc, which is consistent within the errors from the one in the major axis based on Gaussian fits in the uv -plane. The slightly larger sizes in the major axis as opposed to the one from the curve-of-growth (median $\{r_{e,\text{maj},870,\text{uv}}/r_{e,870,\text{cog}}\} = 1.1$) are consistent with the fact that the FIR continuum is not circular in morphology, but it is elongated (Fig. 1).

To assess whether there is any missing flux that is resolved out in the higher-resolution maps, we measured the total fluxes by again using the CASA package IMFIT assuming Gaussian profiles and by comparing the results to the total fluxes measured in visibility. We find that the flux ratios of all six SMGs are consistent with unity to within 1σ with a mean ratio of 1.1 ± 0.1 . We therefore conclude that no significant flux is missing at $\sim 0''.2$ spatial resolution to within 10%, which is consistent with the findings of Hodge et al. (2016).

4. Discussions

4.1. Size measurements

In Sect. 3 we present sizes for both the FIR continuum and H α . Now, we compare our results to those in the literature. We note that while we show that all methods of deriving sizes reach

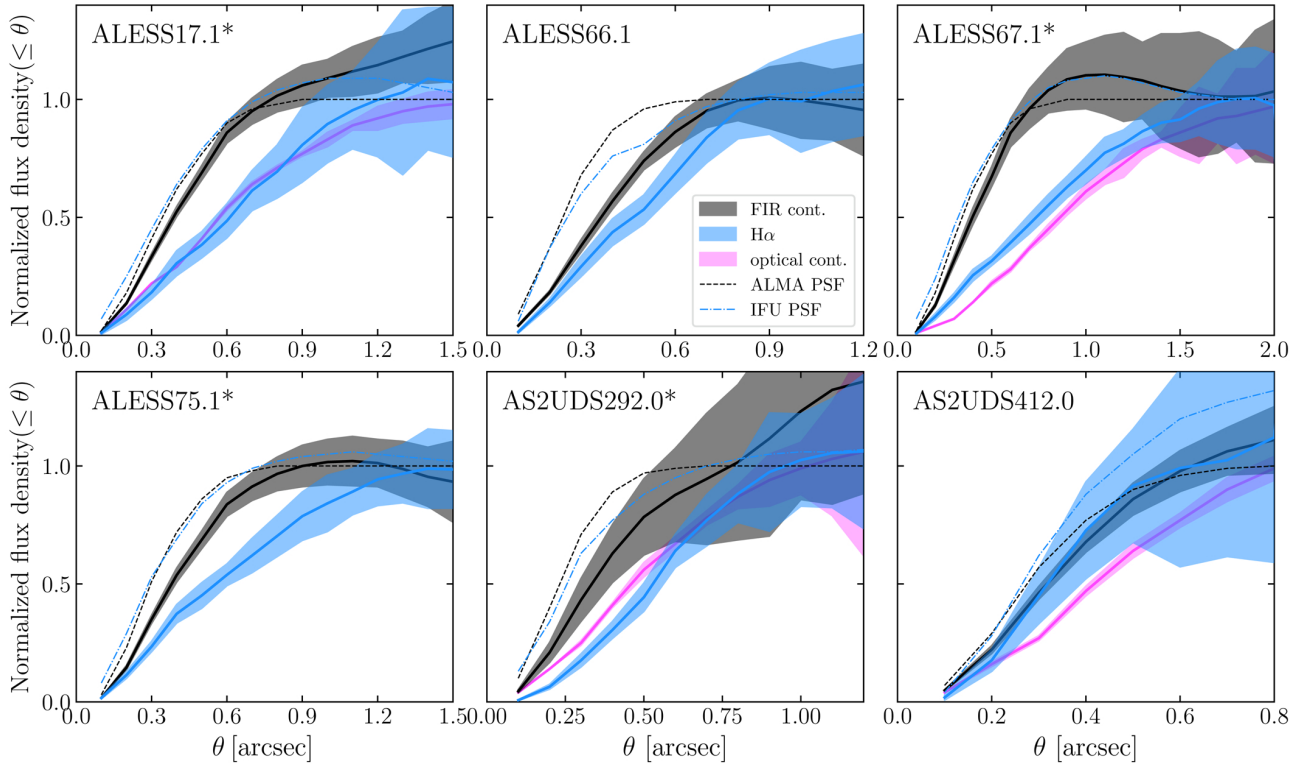


Fig. 2. Curve-of-growth for each of our sample SMGs, showing the rest-frame FIR continuum in black, $H\alpha$ in blue, and wherever available rest-frame optical continuum from HST in magenta. Sources that are identified to host an AGN are marked with an asterisk after the ID. The flux densities were normalized to the total flux densities, and the 1σ uncertainties are shown as respective color bands. All FIR and optical continuum images were convolved to a resolution that matches that of the $H\alpha$ images. The curve-of-growth results for the PSFs are also shown as dashed curves, which are based on the synthesized beam for ALMA and the standard stars for the IFU data.

Table 2. FIR continuum and $H\alpha$ measurements of our sample.

ID	Redshift	F_{870} ^(a) [mJy]	$F_{H\alpha}$ ^(b) [$1E-16 \text{ erg s}^{-1} \text{ cm}^{-2}$]	$r_{e,\text{maj},870,\text{uv}}$ ^(c) [kpc]	$r_{e,870,\text{cog}}$ ^(d) [kpc]	$r_{e,\text{maj},H\alpha,\text{galfit}}$ ^(e) [kpc]	$r_{e,H\alpha,\text{cog}}$ ^(f) [kpc]	r_e ratio ^(g)
ALESS17.1	1.5392(2)	8.2(0.2)	0.6(0.2)	1.7(0.1)	1.7(0.2)	4.3(0.3)	4.5(0.7)	3.0(0.6)
ALESS66.1	2.5534(2)	2.7(0.1)	1.5(0.3)	3.1(0.1)	2.2(0.2)	3.9(0.2)	3.2(0.5)	1.3(0.3)
ALESS67.1	2.1228(6)	3.7(0.2)	2.6(0.4)	1.7(0.1)	1.8(0.3)	4.9(0.2)	5.7(0.5)	3.4(0.7)
ALESS75.1	2.5468(3)	2.6(0.2)	3.4(0.5)	1.7(0.2)	1.9(0.2)	4.0(0.2)	4.0(0.6)	2.1(0.3)
AS2UDS292.0	2.1822(1)	3.1(0.4)	1.0(0.2)	3.1(0.4)	2.0(0.7)	4.3(0.2)	3.9(0.3)	1.8(0.5)
AS2UDS412.0	2.5217(8)	3.7(0.2)	0.5(0.2)	1.5(0.1)	1.3(0.3)	2.7(0.3)	1.5(0.8)	1.1(0.5)

Notes. Uncertainties are given in the parentheses. ^(a)Total $870 \mu\text{m}$ continuum flux density estimated from Gaussian fits in the visibility domain. ^(b)Total $H\alpha$ flux density. ^(c)Half-light radius in major axis at $870 \mu\text{m}$ obtained from CASA fitting in the visibility domain. ^(d)Half-light radius at $870 \mu\text{m}$ obtained from the curve-of-growth analyses based on the ALMA continuum imaging. ^(e) $H\alpha$ half-light radius in major axis obtained using GALFIT based on the 2D emission line intensity maps. ^(f) $H\alpha$ half-light radius obtained from the curve-of-growth analyses based on the IFU cubes. ^(g) $H\alpha$ over $870 \mu\text{m}$ continuum size ratio from which the sizes from the curve-of-growth method are adopted.

consistent results, for uniformity, from now on we adopt the values obtained from the curve-of-growth method, which is model independent and allows for consistent measurements on both data sets.

Our size measurements of the observed $850 \mu\text{m}$ continuum are in agreement with those reported by Hodge et al. (2016), who measured sizes on a larger sample of ALESS SMGs, as well as Simpson et al. (2015), who measured sizes on a subsample of the brighter SMGs in the AS2UDS sample. The finding of sizes between 1–2 kpc is also consistent with studies in other samples of dusty galaxies at $z > 1$ (e.g., Ikarashi et al. 2015; Spilker et al. 2015; Tadaki et al. 2017a; Fujimoto et al. 2018), regardless of them being on the stellar mass and SFR main sequence or not.

The median $H\alpha$ size of our SMG sample, 3.9 ± 0.3 kpc, is consistent with other SMG samples (e.g., Alaghband-Zadeh et al. 2012), but it is significantly larger than those reported based on other star-forming galaxy samples at $z \sim 2$, such as the $H\alpha$ emitters (e.g., median 2.4 ± 0.1 kpc by Molina et al. (2017) or optical and NIR continuum selected samples (e.g., median 2.5 kpc by Förster Schreiber et al. (2018)). However, since, on average, the size of $H\alpha$ agrees with that of optical continuum (Förster Schreiber et al. 2018) and the size of optical continuum positively correlates with the stellar mass (e.g., van der Wel et al. 2014), this discrepancy can be explained by the fact that our sample of SMGs are more massive ($\sim 10^{11} M_{\odot}$) than those from the other galaxy samples ($\sim 10^{10} M_{\odot}$).

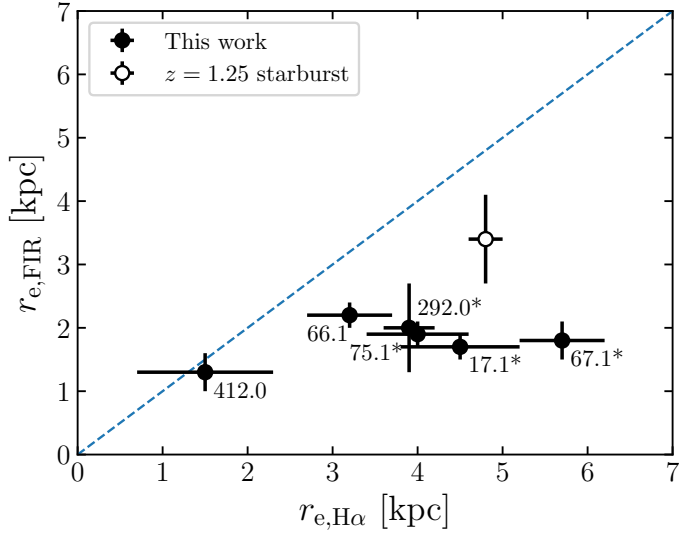


Fig. 3. Comparison between the sizes of H α and those of the rest-frame FIR continuum. Our sample of SMGs are plotted with filled symbols along with their IDs, which have their field names removed for clarity. Sources that are identified to host an AGN are marked with an asterisk after the ID. We also plotted the measurements, which were recently presented by Nelson et al. (2019), of a starburst galaxy at $z = 1.25$ with an empty symbol. Based on our sample of SMGs, we find on a median H α -to-FIR size ratio of 2.0 ± 0.4 with a bootstrapped uncertainty.

The sizes of the FIR continuum and H α from our sample of SMGs, as well as one dusty galaxy at $z = 1.25$ that also has size measurements in both FIR continuum and H α (Nelson et al. 2019), are compared in Fig. 3 in which a clear size difference is shown. In all cases, H α emission appears larger than the FIR continuum (half differ by $>3\sigma$), with a maximum H α -to-FIR size ratio of over three. On average, the size difference in our sample is a median factor of 2.0 ± 0.4 with a bootstrapped uncertainty.

Interestingly, we find that SMGs hosting AGN tend to have larger size ratios, prompting the question of whether AGN are driving the larger H α -to-FIR size ratios. For the three X-ray AGN, we can infer the expected H α luminosities contributed by the AGN by adopting the $L_X-L_{H\alpha}$ correlation deduced by Ho et al. (2001) based on samples of nearby AGN, and we find that $\lesssim 10\%$ of the measured H α luminosities are contributed by AGN. In addition, the low [N II]-to-H α ratios in all of our sample SMGs, in particular from the outskirts, suggest that the ionizing conditions are consistent with those of H II regions and that H α can be mainly attributed to star formation and not AGN. Finally, there is currently no evidence, including from our sample, suggesting that the FIR continuum sizes depend on the presence of an AGN (e.g., Harrison et al. 2016).

On the other hand, recently, a similar study by Scholtz et al. (2020) on a sample of eight X-ray selected AGN at $z \sim 2$ with strong H α and [O III] lines has also found a similar H α -to-FIR size ratio of 2.3 ± 0.3 . This evidence could suggest that somehow AGN are driving the larger H α sizes, or it could be that this is a general feature of FIR luminous galaxies at $z \sim 2$ and the current studies are biased toward galaxies hosting AGN because of their brightness in strong optical lines. Nevertheless, a systematic study on a larger sample, especially including more FIR luminous sources without hosting AGN, is clearly needed to investigate this further.

The larger H α size over FIR continuum in $z \sim 2$ dusty star-forming galaxies is somewhat expected according to recent stud-

ies in the literature comparing either FIR and rest-frame optical continuum or H α and rest-frame optical continuum. For example, Hodge et al. (2016) find that the rest-frame optical continuum of their sample of ALESS SMGs is about three times larger than the FIR continuum. This size difference of a factor of 2–3 is almost universally observed in both other similarly FIR-luminous galaxies (e.g., Barro et al. 2016; Elbaz et al. 2018) and less FIR-luminous star-forming galaxies at $z \sim 2$ (e.g., Tadaki et al. 2017a; Fujimoto et al. 2018).

On the other hand, using AO-aided SINFONI IFU data that are matched in spatial resolution to the HST imaging, Förster Schreiber et al. (2018) show that the H α size of their $z \sim 2$ massive star-forming galaxies is identical to the rest-frame optical continuum on average. Chen et al. (2017) find a similar result on one SMG, ALESS67.1, which is included in our sample. Four of our sample SMGs have HST H -band imaging, and the results of the curve-of-growth analyses are plotted in Fig. 2. On average, we find a H α -to-optical size ratio of 1.0 ± 0.1 .

All of these results suggest that, on average, H α is similar in size to the rest-frame optical continuum and both are a factor of 2–3 larger than the FIR continuum. The much smaller size of FIR continuum compared to almost any other tracer, including molecular gas (e.g., Ginolfi et al. 2017; Chen et al. 2017; Calistro Rivera et al. 2018), challenges the typical assumption regarding the treatment of dust attenuation in the SED modeling (e.g., Simpson et al. 2017). In the following sections, we investigate and discuss some possible implications in detail.

4.2. Star-formation rates

There are a few possible implications because of the size difference between FIR continuum, H α , and optical-to-infrared (OIR) continuum. We start with the measurements of SFRs. It is important to note the UV-to-NIR photometry of ALESS66.1 is contaminated by a nearby quasar at $z = 1.31$ (Simpson et al. 2014; Danielson et al. 2017). We therefore exclude it from the analyses from now on.

4.2.1. Dust correction of H α

Under the assumption that the total SFRs can be estimated through either attenuation-corrected H α or UV-to-FIR continuum photometry, one possible implication of the size difference has to do with the attenuation correction of H α -based SFRs, particularly in cases where FIR measurements are not available. To account for dust attenuation, a typical approach is to assume a foreground dust screen, which is cospatial in the projected sky with the underlying UV and optical star-formation tracers. This is one of the fundamental assumptions of some of the popular SED modeling involving corrections of dust attenuation, including HYPERZ (Bolzonella et al. 2000) and EAZY (Brammer et al. 2008). However with spatial mismatches between H α and FIR continuum, these assumptions need to be further examined and the possible impact needs to be understood.

To understand such an impact, if any occurred, we first aim to compare the attenuation-corrected H α -based SFRs and the dusty SFRs derived from the total infrared luminosities. That is, instead of adopting the energy-balance approach, we modeled the UV-to-NIR and MIR-to-radio SEDs separately. Thus we mimicked the traditional approach of deriving total SFRs without FIR measurements and then used the FIR-inferred SFRs to validate this approach. In principle, a significant size difference between dust and H II regions may result in either the attenuation-corrected H α -based SFRs being systematically

lower than the dusty SFRs, both measurements being uncorrelated, or both.

To obtain the attenuation-corrected $H\alpha$ SFRs, the best approach is to also measure the $H\beta$ luminosity and estimate the nebular attenuation through the Balmer decrement (e.g., Reddy et al. 2015). However, $H\beta$ is only available in a marginal detection from one SMG, ALESS75.1. To be able to apply a consistent methodology across the sample, alternatively, we opted to use the stellar attenuation derived from the UV-to-NIR SED fitting. We note that further corrections on top of the stellar attenuation may need to be applied (e.g., Calzetti et al. 2000; Wuyts et al. 2013; Price et al. 2014).

In order to model the UV-to-NIR SEDs, we used HYPERZ (Bolzonella et al. 2000), which is a χ^2 minimization code, to fit a set of model SEDs on the observed photometry. The model SEDs are based on synthetic SED templates whose intrinsic shape is characterized by the star-formation history (SFH). The synthetic SEDs are further modified according to dust reddening, Lyman forest, and redshifts. The four synthetic SED templates considered were created with the spectral templates of Bruzual & Charlot (2003), assuming the following solar metallicities with different SFHs: a single burst (B), two exponentially decaying SFHs with timescales of 1 Gyr (E) and 5 Gyr (Sb), and constant star formation (C). The undetected photometric measurements were set to a flux of zero with uncertainties equal to 1σ of the limiting magnitude of that filter. We followed the Calzetti et al. (2000) law to allow total attenuation (A_V) between 0 and 5 in steps of 0.01. The age of the galaxy must be younger than the age of the Universe.

Our methodology is similar to that of Simpson et al. (2014), who also conducted HYPERZ fitting on ALESS SMGs. However they did not have full spectroscopic redshift information. Therefore, for verification purposes, we first compared our fitting results of the ALESS SMGs against those of Simpson et al. (2014) by allowing the redshift to vary between 0 and 6 in steps of 0.1. We confirm that we were able to reproduce their results. We then determined A_V by setting the redshift range to the spectroscopic redshifts with uncertainties measured from $H\alpha$. We find that under one synthetic SED template, A_V are always invariant within the spectroscopic redshift uncertainties (we adopt $\pm 3\sigma$). However, the variations become significant from template to template, namely they are affected by the SFHs adopted. We, therefore, performed fits by considering one SED template at a time and we took all of the A_V values from fits that have $\Delta\chi^2 < 1$ from the lowest χ^2 . When deriving the dust-corrected SFRs, we propagated the range of these A_V values into the uncertainties. We find typical A_V values of 1–3 for SED sampled down to the rest-frame UV, which is consistent with previous findings of SMGs (Takata et al. 2006; Wardlow et al. 2011; Simpson et al. 2014; da Cunha et al. 2015).

We now move on to the fitting of the FIR SEDs. We adopt the approach of template fitting. In particular, we used the library of 185 template SEDs constructed by Swinbank et al. (2014), who included local galaxy templates from Chary & Elbaz (2001), Rieke et al. (2009), and Draine et al. (2007), as well as the SEDs of the well-studied high-redshift starbursts SMM J21350102 ($z = 2.32$) and GN20 ($z = 4.05$) from Ivison et al. (2010) and Carilli et al. (2011), respectively. The MIR-to-radio photometry of the ALESS SMGs, including MIPS 24, PACS 70 and 160 μm , SPIRE 250, 350, and 500 μm , ALMA 870 μm , and VLA 1.4 GHz, were derived by Swinbank et al. (2014). The same methodology was applied to the AS2UDS SMGs (Stach et al. 2019). We fit the MIR-to-radio photometry using χ^2 minimization and adopted the spectroscopic redshifts measured by our

IFU observations. We then derived the infrared luminosity by integrating the best-fit template SED as well as all acceptable SEDs based on their χ^2 values, over the rest-frame 8–1000 μm range.

Having the fitting results in hand, we estimated the SFRs based on $H\alpha$ and infrared luminosities by adopting the calibration provided by Kennicutt & Evans (2012)⁴. We plotted the results in Fig. 4. First, we find that the $H\alpha$ -based SFRs without attenuation correction are on average a factor of 21 ± 15 in median (with bootstrap error) lower than infrared-based SFRs. Similar discrepancies have been reported in other SMG samples (Swinbank et al. 2004; Casey et al. 2017). We then corrected the $H\alpha$ luminosities using the stellar attenuation via $L_{H\alpha} = L_{H\alpha, \text{obs}} \times 10^{0.4A_{V, \text{star}}}$ in which $A_{V, \text{star}}$ was obtained through the UV-to-NIR HYPERZ fitting. After correcting for dust attenuation, the infrared SFRs are still systematically higher, but now by a factor of 4 ± 2 .

The systematically lower $H\alpha$ -based SFRs correct for stellar attenuation and, given the assumption that the total SFRs can be obtained from either infrared luminosity or attenuation-corrected $H\alpha$, this suggests that an additional correction on top of the stellar attenuation is needed for $H\alpha$. On the other hand, if the discrepancy persists after further corrections, the aforementioned assumption may be challenged and it could suggest that the bulk of the dusty star formation may not be traced through rest-frame optically detectable regions, including H II regions, as partly supported by our findings on size difference.

To assess the amount of further correction, we now look at the possible differences between nebular and stellar attenuation. Using the Balmer decrement, the comparison of the two has been extensively studied in both local samples (Calzetti et al. 2000; Wild et al. 2011; Kreckel et al. 2013) and higher redshifts (Kashino et al. 2013; Price et al. 2014; Reddy et al. 2015; Theios et al. 2019). In particular, the seminal work of Calzetti et al. (2000) found that by using a sample of local starbursting galaxies, the nebular attenuation was larger with a relation of $E(B - V)_{\text{star}} = 0.44E(B - V)_{\text{neb}}$. However, a variety of results have been found in other samples. While the consensus has yet to be reached since the relation likely depends on galaxy properties (Wild et al. 2011; Price et al. 2014; Puglisi et al. 2016), there is growing evidence showing that at $z > 1$, between the nebular and stellar attenuation, the discrepancy appears to be smaller but the correlation is scattered (Kashino et al. 2013; Reddy et al. 2015; Puglisi et al. 2016; Theios et al. 2019).

For this exercise, we adopt two representative results from Calzetti et al. (2000) and Kashino et al. (2013), as the former represents the largest discrepancy between nebular and stellar attenuation found so far, and the latter presents a galaxy sample that has properties closer to those of our sample in redshift,

⁴ The conversion from infrared luminosities to SFRs heavily depends on the star-formation history, which varies by a factor of around five given different star-formation timescales (Calzetti 2013). Ideally, one should adopt the conversion based on the best-fit SED template from HYPERZ. However, as shown in previous studies of SMGs, the UV-to-NIR continuum tends to be spatially offset from the FIR continuum (Chen et al. 2015; Hodge et al. 2016). Therefore, the star-formation history derived from UV-to-NIR photometry likely does not reflect the true star-formation history in the dust regions emitting FIR continuum. The conversion from Kennicutt & Evans (2012) roughly represents the mean value of the possible range provided by Calzetti (2013). We, therefore, expect that the uncertainty of the conversion due to unknown star-formation history contributes mostly to the scatter of the correlation, and not the normalization.

stellar mass, and SFR. Calzetti et al. found $E(B - V)_{\text{star}} = 0.44 \pm 0.03E(B - V)_{\text{neb}}$ and Kashino et al. find $E(B - V)_{\text{star}} = 0.70 \pm 0.08E(B - V)_{\text{neb}}$ ⁵.

Given $A_{\lambda} = \kappa(\lambda)E(B - V)$ in which $\kappa(\lambda)$ is the attenuation curve⁶, we deduce a total attenuation relation of $A_{\text{H}\alpha} = 1.4 \pm 0.1A_{V,\text{star}}$ and $A_{\text{H}\alpha} = 0.9 \pm 0.1A_{V,\text{star}}$ based on the result of Calzetti et al. (2000) and Kashino et al. (2013), respectively. We applied the relation to our measurements and plotted the results in Fig. 4.

Despite applying further corrections, the attenuation-corrected H α -based SFRs still cannot account for all of the SFRs revealed in the infrared; they miss at least a median factor of 3 ± 1 considering the most aggressive correction based on the Calzetti attenuation curve. The Spearman correlation coefficient is 0.6 ($p = 0.2$), so the two SFRs appear to be possibly correlated among these five galaxies. However, given the discrepancy between the two SFRs even after accounting for attenuation for H α , the correlation could be driven by the global properties of the galaxy, such as gas fraction or the dynamical environment, instead of them tracing the same part of star-forming regions, which is partially supported by our findings on the size difference between the two SFR tracers. Instead of acting as a foreground screen, it is also possible that dust is spatially mixed with H II regions and that dust column density reaches a level at which H α becomes optically thick, in particular, in the central regions. Thus, H α does not reflect the full attenuation. Evidence of this possibility has been shown in studies of (U)LIRGs, where the attenuation derived from Pa α /Br γ or Br γ /Br δ in near-infrared is slightly higher than what is derived from Balmer decrement (e.g., Piqueras López et al. 2013). Interestingly, for the local ULIRGs there is also evidence showing that their IR-based SFRs are higher than the attenuation-corrected, H α -based SFRs, by a factor of 2–30 (García-Marín et al. 2009). In the next section, we further investigate the reasons driving the mismatching SFRs and, in particular, the size difference between FIR continuum and H α .

4.2.2. Total star-formation rates

In Sect. 4.2.1, we discuss the implications due to the spatial mismatches between the FIR continuum, H α emission, and optical continuum. In particular, when considering SFRs, the attenuation corrected H α -based SFRs are systematically lower than the IR-based SFRs. Given that the total SFRs at high redshifts are frequently either derived from IR+UV⁷ or attenuation corrected H α (e.g., Shivaie et al. 2016), the discrepancy merits further discussion. We explore two closely related issues regarding the following: the attenuation correction and the spatial mismatches between the bulk of dust and the H II regions.

On the attenuation correction, in order to align both SFRs, the correction needs to be about 50% more on top of the extra correction provided by Calzetti et al. (2000), which is similar to

⁵ The original relation found by Kashino et al. (2013) is $E(B - V)_{\text{star}} = 0.83 \pm 0.1E(B - V)_{\text{neb}}$, which explicitly assumes a Calzetti attenuation curve on both Balmer decrement and stellar continuum. However, Calzetti et al. (2000) adopted the Calzetti attenuation curve for the stellar continuum but a Milky Way attenuation curve on H α (Cardelli et al. 1989). We, therefore, converted the Kashino et al. result based on the same assumption of the attenuation curves used in Calzetti et al. (2000).

⁶ We note that $\kappa(\text{H}\alpha; 6565 \text{ \AA}) = 2.54$, assuming the Milky Way attenuation curve (Cardelli et al. 1989), and $\kappa(V; 5530 \text{ \AA}) = 4.02$, assuming the Calzetti attenuation curve.

⁷ In our case, UV-based SFRs are $\sim 1\%$ of IR-based SFRs, so they are negligible.

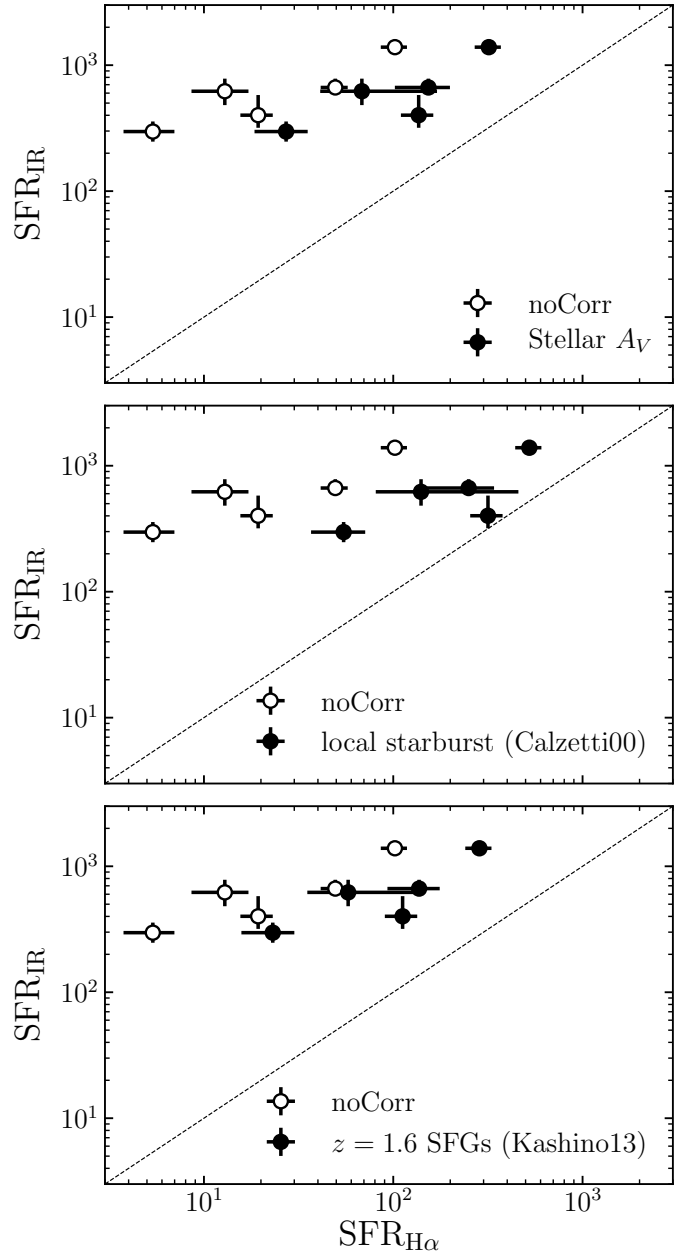


Fig. 4. Comparison between the IR-based SFRs and the H α -based SFRs, except for ALESS66.1, where the UV-to-NIR photometry is contaminated by a foreground nearby quasar. The derivations of SFRs are described, in detail, in Sect. 4.2.1. In each panel, the empty symbols are plotted based on the measured H α -based SFRs without attenuation correction (noCorr), and the filled symbols are plotted based on the H α -based SFRs corrected for attenuation using various methods: In the *top panel*, we adopt the stellar A_V derived from the SED fitting; in the *middle and bottom panels*, we adopt the attenuation of the H II regions based on a fractional correction to the stellar A_V provided by Calzetti et al. (2000) and Kashino et al. (2013), respectively. While the exact amount of correction for attenuation is still under debate, we find that even if we adopt the largest correction provided by Calzetti et al. (2000), the H α -based SFRs are still a factor of 3 ± 1 lower than the IR-based SFRs on average.

what Wuyts et al. (2013) find. However, such an aggressive correction based on the Balmer decrement has never been observed (e.g., Price et al. 2014). In fact, studies of $z \sim 2$ star-forming galaxies find the opposite with significantly smaller values (e.g., Kashino et al. 2013; Reddy et al. 2015). We do note that these

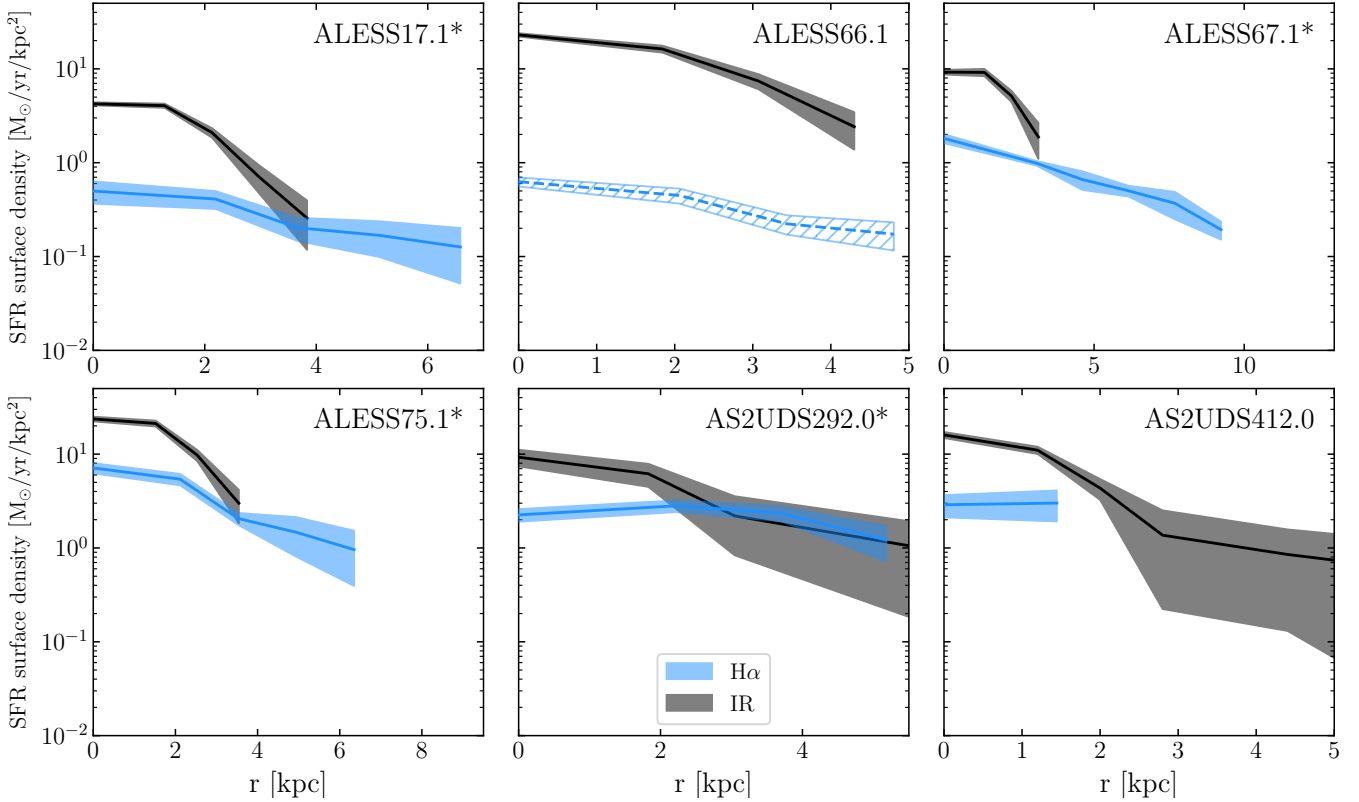


Fig. 5. SFR density profiles based on the curve-of-growth analyses (Fig. 2), which were deconvolved according to the PSF. Sources that are identified to host an AGN are marked with an asterisk after the ID. For the IR-based profiles, we assume that they follow the morphology of the observed $870\ \mu\text{m}$ emissions, meaning the IR-based SFRs in each radial bin is the fraction of the total $870\ \mu\text{m}$ flux times the total SFRs. The $\text{H}\alpha$ -based profiles were derived by differentiating the curve-of-growth results, converting the $\text{H}\alpha$ luminosity to SFRs according to Kennicutt & Evans (2012), and adopting an attenuation correction of Calzetti et al. (2000), except for ALESS66.1 for which the OIR photometry is contaminated by a foreground quasar (Fig. 1). For ALESS66.1, we plotted the profile without correcting for attenuation. For clarity, we only plotted the bins that have $\geq 1\sigma$ measurements.

studies mostly focus on less obscured, lower stellar mass, and lower SFR galaxies in comparison with our sample SMGs. However, if the IR-based and $\text{H}\alpha$ -based SFRs would have indeed been matched, it would have suggested that, in general, the relation between the nebular A_V and stellar A_V is very different in the SMGs compared to that in the more typical star-forming galaxies. A more likely situation is that the bulk of the obscured star formation is not traced by either the $\text{H}\alpha$ or stellar emissions, which is due to a combination of a few factors including a global-scale size difference and very high obscuration in the central dusty regions. In the following, we discuss these two possibilities further.

One way to quantify to what extent the global-scale size difference plays a role is to estimate how much of the $\text{H}\alpha$ -based SFRs originate from outside the bulk of dust as traced by the FIR continuum. Our data allow for a simple 1D assessment. To do so, in Fig. 5 we plotted the SFR densities as a function of radial distances based on the FIR and $\text{H}\alpha$ measurements. Since, we do not have spatially resolved information as to the other FIR bands, we assume that the IR-based SFR density profile follows the morphology of the observed $870\ \mu\text{m}$ emissions, as derived from the curve-of-growth analyses. That is, the IR-based SFRs in each radial bin is the fraction of the total $870\ \mu\text{m}$ flux in that bin multiplied by the total SFRs. This method effectively assumes a constant dust temperature and dust opacity, which is likely not true since evidence of a negative temperature gradient (hot to cold from the center to the outskirts) has recently been found in

SMGs (Calistro Rivera et al. 2018). However, a negative gradient of dust temperature would mean an even more compact SFR density distribution.

For the $\text{H}\alpha$ profiles, we simply differentiated the curve-of-growth results, converted the $\text{H}\alpha$ luminosities to SFRs according to Kennicutt & Evans (2012), and adopted the stellar A_V with a further correction to the nebular A_V based on Calzetti et al. (2000), except for ALESS66.1 for which the OIR photometry is contaminated so it is excluded in discussions that follow. We note that the total attenuation is based on integrated photometry, so the correction is the same across all radial bins. While it is expected that the total attenuation has a negative gradient so is higher in the central regions (Wuyts et al. 2012; Nelson et al. 2016; Liu et al. 2017), the total attenuation derived from the integrated photometry likely reflects the averaged conditions across the whole galaxy. We discuss the consequences of this scenario in detail in the following paragraphs. Finally, to show the intrinsic distributions, all profiles were deconvolved in quadrature according to the PSF.

For the simplest quantification, we find that the fraction of $\text{H}\alpha$ -based SFRs that are located outside the central dusty regions ranges from zero (AS2UDS412.0) to 40% (ALESS67.1). The fraction would decrease if there is a negative gradient of A_V , but increase with a negative gradient of dust temperature. We also note that different centroids are adopted for $870\ \mu\text{m}$ continuum and $\text{H}\alpha$ in the curve-of-growth analyses (Fig. 1), which has, however, a negligible impact such that the fraction would

only increase by a maximum of 5% if the same centroids had been adopted. While it appears from this exercise that in the 1D profile the H α -based SFRs are more extended relative to the FIR-based SFRs, the bulk of H α -based SFRs spatially overlap with the FIR-based SFRs. That is, the size difference in the global scale between the FIR continuum and H α is not the dominant factor that drives the mismatching SFRs estimated by these two SFR tracers. The dominant factors are likely linked to heavy dust attenuation in the central regions.

By estimating the hydrogen column density through dust masses and FIR continuum sizes, [Simpson et al. \(2017\)](#) find that by assuming a foreground screen of dust geometry, the averaged total attenuation in the central dusty regions of SMGs is $A_V = 540^{+80}_{-40}$, suggesting that indeed all of the optical-infrared (OIR) emission that is spatially coincident with the far-infrared emission region is completely extinguished by dust. In addition, in the most recent work by [Hodge et al. \(2019\)](#) at a spatial resolution of ~ 500 pc, they find that the FIR continuum of SMGs becomes clumpy and structured in shapes of spiral arms, bars, and rings. In such a case, the total attenuation of the dusty regions could exceed the values estimated by [Simpson et al. \(2017\)](#), suggesting that the bulk of the dusty star formation as traced by FIR continuum is spatially decoupled from H α on sub-kpc scales. If we take the median value from [Simpson et al. \(2017\)](#), which is $A_V = 540$, and apply the correction to the H α -based SFRs, the resulting SFRs would be on the order of $10^{0.4 \times 540} \sim 10^{216} M_\odot \text{ yr}^{-1}$, which is unrealistic. It would still be unrealistically high if we were to only apply this correction at the central regions where most of the dust is located.

On the other hand, another possibility could be that instead of acting as a foreground screen, the dust is mixed with the H II regions. In this case, the FIR continuum would not be spatially decoupled from H α ; however, given the high column density, H α is no longer optically thin and, therefore, it does not reflect the total attenuation. Both scenarios would lead to a significant underestimation of the total SFRs from H α . More data on IR continuum along with the Balmer and even the Paschen lines with very high angular resolutions ($< 0.1''$), presumably from ALMA and ELT, should shed more light on this issue.

4.3. SED modeling and dust distribution

Another possible implication of a size difference is the SED modeling and, in particular, those employing the energy-balance approach. We now discuss this aspect in detail.

4.3.1. Comparison to the energy balance approach

The spatial mismatch we see between dust and OIR emission may have implications for energy balance SED modeling. In particular, for our sample of SMGs, one can imagine that because the majority of dust is not collocated with the OIR emissions, the attenuation estimated from OIR alone may be less than the attenuation derived from the energy balance approach. That is, the energy balance fitting may deduce a higher attenuation solution in the OIR in order to provide a better fit to the FIR photometry and, in particular, for high luminosity sources. To test this possibility, we also modeled our UV-to-radio SEDs by using the MAGPHYS code. We adopt the high- z edition, which includes the modeling in the radio bands, as well as the Lyman absorptions in the rest-frame UV from the intergalactic medium ([da Cunha et al. 2015](#)). We plotted the best-fit models in Fig. 6, along with the photometric measurements, and the fitting results of HYPERZ and those using the infrared templates.

We first compare the infrared luminosities estimated from the SED templates⁸ and those from MAGPHYS. We confirm that both values are statistically consistent with each other in all sources. We then turn to A_V in which we find significant differences in some sources. As seen in Fig. 6, ALESS67.1, ALESS75.1, and AS2UDS412.0 appear to have different best-fit models in the UV-to-NIR regime, although the fit from HYPERZ shows better agreement with the data. Interestingly, in these three cases where the A_V differ, the values obtained from MAGPHYS are all higher.

We note that given the different assumptions of the attenuation curves in these two codes, the A_V values from the UV-to-NIR regime should also ideally be deduced from MAGPHYS by turning off the fitting of the MIR-to-radio part. Unfortunately, the public version of MAGPHYS does not support this option. However, the fact that the A_V values are in excellent agreement with each other in ALESS17.1 and AS2UDS292.0, which is as expected from a good match shown in Fig. 6, suggests that the systematic difference between the A_V values can be neglected. We also tried to homogenize the two codes by running the HYPERZ fitting that only uses the τ -decay SFHs that are similarly adopted by MAGPHYS, thus definitively removing the bursting SFH in our adopted method for HYPERZ. We find that the output values vary within uncertainties and the conclusions remain unchanged. Since stellar mass is not one of the direct outputs from HYPERZ, we estimated the stellar masses by converting the absolute magnitude, which is one of the outputs from HYPERZ based on some estimates of mass-to-light ratios. In particular, we used the H -band absolute magnitude from HYPERZ and the mass-to-light ratios from [Simpson et al. \(2014\)](#) where the ratios were derived based on the [Bruzual & Charlot \(2003\)](#) simple stellar population models. We find that all but one (AS2UDS292.0) of their stellar mass estimates from the two codes are in agreement with each other within uncertainties. The disagreement with AS2UDS292.0 is mainly caused, as expected, by the fact that the HYPERZ fitting finds the best solution based on the bursting SFH. If we force a τ -decay-like fitting, then the stellar mass estimated from HYPERZ agrees with that from MAGPHYS, with a little change in A_V so again the conclusions are not sensitive to this change.

To further understand what causes the different A_V values, we first plotted the A_V ratios as a function of the size ratios between H α and the FIR continuum in Fig. 7. Naively, one may expect that better agreement in spatial distribution between dust and the OIR emissions would lead to better agreement in A_V . That is, the more the sizes differ, the more the A_V differs. Interestingly, we do not observe such a trend. Instead, we find a more prominent correlation between the A_V ratios and the total infrared luminosity (Fig. 7). While a larger sample is clearly needed to confirm this, this correlation may suggest that the energy balance approach does indeed deduce a higher A_V in cases of high infrared luminosity, sacrificing a poorer fit in the UV-to-NIR in return for an overall smaller χ^2 value.

It is understandable that the discrepancy is the largest toward the higher infrared luminosity end, especially when the infrared luminosity is so high that the best-fit UV-to-NIR models cannot account for it. On the other hand, the more interesting question is perhaps why the A_V values are in agreement in the lower infrared luminosity end, despite the spatial mismatches. Based on [da Cunha et al. \(2008, 2015\)](#), MAGPHYS adopts a two-component model (birth cloud and diffuse ISM) to describe the attenuation of stellar emission at the UV-to-NIR regime.

⁸ The total infrared luminosity given by MAGPHYS is integrated over 3–1000 μm . We, therefore, adopted the same wavelength range to compute the total infrared luminosity from the best-fit SED templates.

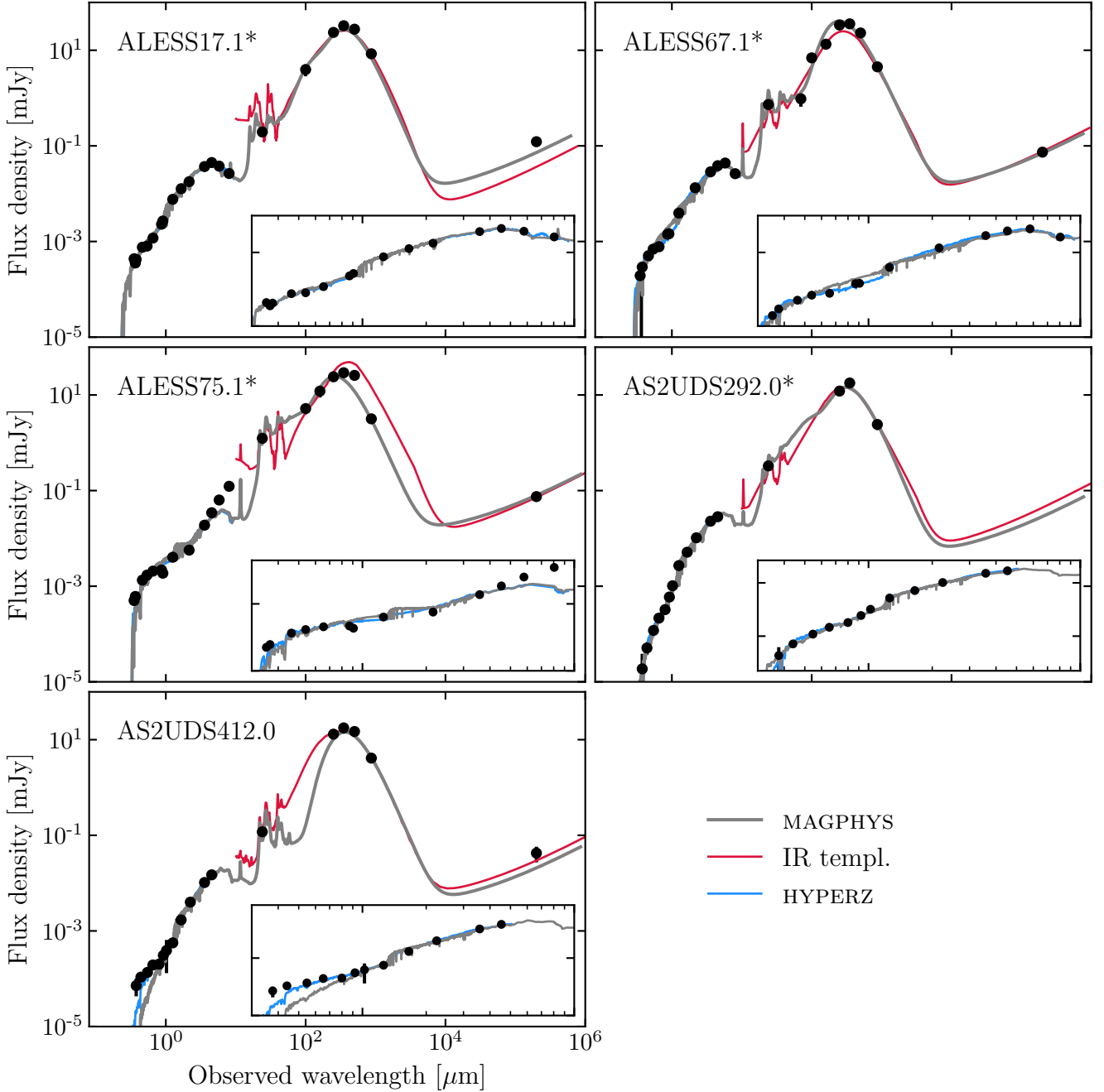


Fig. 6. UV-to-radio SEDs for each of our sample SMGs except ALESS66.1 for which the UV-to-NIR photometric measurements are contaminated by a foreground quasar [Simpson et al. \(2014\)](#). Sources that are identified to host an AGN are marked with an asterisk after the ID. The measurements are plotted as black points and the best-fit models from MAGPHYS, HYPERZ, and the IR templates compiled by [Swinbank et al. \(2014\)](#) are plotted as gray, blue, and red curves, respectively. For clarity, we do not show the uncertainty, however, it is discussed in the text, including the fact that the IR luminosities that were estimated by the two methods are in agreement with each other within the uncertainty. The insets are zoom-ins in the OIR regime from 0.3 to 10 μm in log–log scale. We find significant differences in higher L_{IR} sources between the best-fit models of MAGPHYS and HYPERZ; also, in all of these discrepant cases, the HYPERZ modeling provides a better fit with a lower χ^2 .

Since the UV-to-NIR emissions largely originate from the stars in the diffuse ISM, it is possible to boost the infrared luminosity by increasing the attenuation in the birth clouds without significantly increasing the total attenuation, which is A_V . Indeed, for the two sources, ALESS17.1 and AS2UDS292.0, where the modeling of HYPERZ and MAGPHYS is in the best agreement, the optical depth seen by the stars in the birth clouds (defined as τ_V in MAGPHYS) is a factor of 2–3 higher than in the rest of the sources, and the fraction of τ_V seen by stars in

the diffuse ISM (defined as μ in MAGPHYS) is a factor of 2–3 smaller. One of the consequences of these ad-hoc tunings is that the infrared emissions from the birth clouds alone, such as the PAH and the MIR emissions, could become unrealistically high. Unfortunately this is the regime where we currently lack data. Future missions targeting MIR, such as JWST and SPICA, will be able to shed more light on this issue.

In short, we find that the level of impact due to spatial mismatches on the energy balance approach of SED modeling

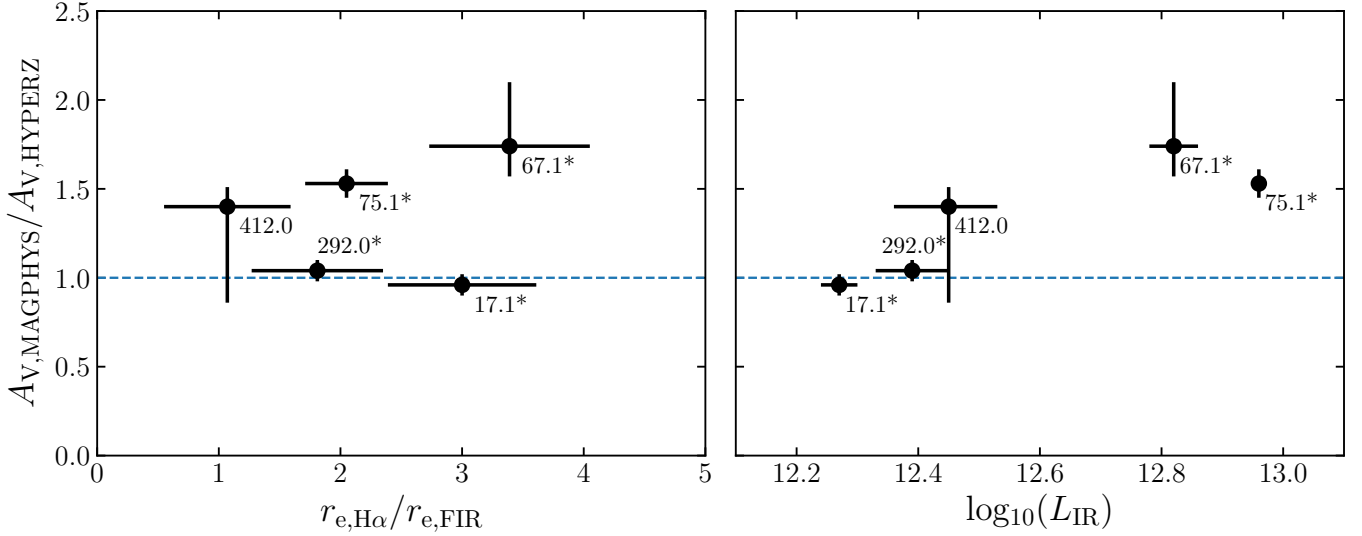


Fig. 7. Comparison of the ratio of the total attenuation derived from the best-fit model of MAGPHYS to that of HYPERZ, the size ratio of H α to the FIR continuum (*left*), and the total infrared luminosity (*right*). Data points are plotted along with their corresponding IDs, which have their field names removed for clarity. Sources that are identified to host an AGN are marked with an asterisk after the ID. We find a correlation between the ratio of attenuation and the infrared luminosity.

depends on the physical properties. For example, they have a negligible impact on the total IR luminosity. However, on the other hand, for IR luminous ($L_{IR} \geq 10^{12.6-12.8} L_{\odot}$) galaxies, significant impact can be seen in total attenuation, which is intrinsically related to stellar age, star-formation history, and stellar mass. For less IR luminous galaxies, the impact could be more subtle, which is possibly related to the fractional contribution of total attenuation between the diffuse ISM and the birth clouds.

4.3.2. Three-component dust distributions

As briefly mentioned in the previous section, it is normally perceived that there are generally the following two main components for dust distribution (or attenuation): the diffuse ISM, which mostly encompasses older stars and older star-forming regions as revealed by the UV radiation, and the birth clouds that mostly trace H II regions where more intensive and younger star formation occurs (Fig. 8; Calzetti et al. 1994). This is the essential assumption some of the SED models adopt, including those that employ the energy balance approach (e.g., MAGPHYS and CIGALE). The advantage of this model, and some variations based on it, can explain most of the observational results regarding the different attenuation observed between H α and the stellar continuum. For example, the generally higher color excess of H α compared to that of stellar continuum is a natural consequence of this model. In addition, the fractional distribution between the birth clouds and the diffuse ISM can explain some correlations between the galaxy properties (i.e., SFR, stellar mass, and specific SFR) and the ratio of nebular to the stellar A_V (e.g., Wild et al. 2011; Price et al. 2014; Reddy et al. 2015).

However, the two-component schematic model is built purely based on the OIR data, without the observational knowledge of the spatial distribution of dust. Through the analyses in Sect. 4.2.2, our data on the six SMGs suggest that the model becomes incomplete once the spatially resolved FIR data are considered; namely, the majority of the dust attenuation cannot be traced via H α or OIR continuum only. A scenario that involves a third component, a centrally concentrated, extremely dusty component, appears more appropriate (Fig. 8). Most of

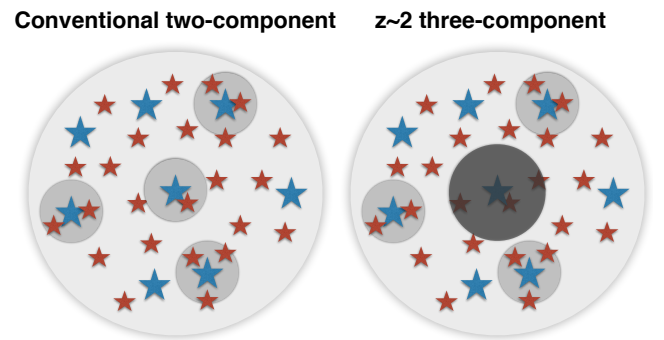


Fig. 8. Schematic figure showing the conventional two-component view of the dust distribution and the postulated three-component model that is supported by our measurements as well as literature studies on some $z \sim 2$ galaxies with lower IR luminosities. The red stars represent older stellar populations that dominate the integrated rest-frame UV to NIR, while the blue stars represent the young star-forming H II regions traced by H α . The gray regions show the rough distributions of dust with the opacity reflecting their total attenuation, meaning that the darker regions are more obscured than the lighter ones.

this third component of high dust concentration has a low filling factor and this is likely not reflected by the rest-frame OIR and H α .

Although this new scenario is based on the data of the six SMGs, it is also supported by other studies in the literature on OIR-selected galaxy samples. For example, Nelson et al. (2019) find insufficient correction of their H α SFR in the central regions of a dusty galaxy at $z = 1.25$ even when having spatially resolved estimates for dust attenuation; this also results in a mismatch between the H α SFR density profile and that of the IR SFRs. Adding this component mitigates the tension between the A_V derived only from OIR photometry and that from the UV-to-radio energy balance modeling. It also naturally explains the mismatch between the H α -based SFRs and the IR-based SFRs on our sample of SMGs. While we lack nebular attenuation measurements through Balmer decrement, which would completely verify this scenario in our sample of SMGs, the recent

study by Scholtz et al. (2020) on a sample of eight ALMA-detected, X-Ray selected AGN confirm that in six of their AGN that have constraints of Balmer decrement, the nebular A_V values are indeed all larger than the stellar A_V values. Together with the fact that they also find a similar FIR continuum to $H\alpha$ size ratio, the results of Scholtz et al. (2020) support the three-component model.

While SMGs can be located on or above the massive end ($\sim 10^{11} M_\odot$) of the main sequence (e.g., Michałowski et al. 2012, 2017; da Cunha et al. 2015), due to their low space density, the contribution of SMGs to the total cosmic SFR density is about 10–30% (Barger et al. 2012; Swinbank et al. 2014; Cowie et al. 2017). Therefore, if the three-component model were to be generalized to the other galaxies at $z \sim 2$, perhaps a more interesting question to pose is whether typical $z \sim 2$ star-forming galaxies that dominate the cosmic SFR density are on average less luminous in the infrared and have a similar FIR-to- $H\alpha$ spatial disparity. A few studies in the literature may give us some hints.

Through FIR measurements of both individual galaxies and stacked images of their ALMA data, it has been found that on average galaxies at $z \sim 2$ are smaller if they have lower infrared luminosities ($\sim 10^{12} L_\odot$ so $\text{SFR} \sim 100 M_\odot \text{yr}^{-1}$; Tadaki et al. 2017a; Fujimoto et al. 2017, 2018). In addition, they also find that the FIR sizes are a factor of 2–3 smaller than the rest-frame optical sizes for galaxies with lower infrared luminosities. In the meantime, using AO-aided SINFONI observations, Förster Schreiber et al. (2018) find that in their sample of $z \sim 2$ star-forming galaxies that have a wide range of stellar masses (2×10^9 – $3 \times 10^{11} M_\odot$, median $\sim 2 \times 10^{10} M_\odot$) and SFRs (10 – $650 M_\odot \text{yr}^{-1}$, median $\sim 80 M_\odot \text{yr}^{-1}$), the stellar sizes are consistent with the $H\alpha$ sizes to within about 5% on average. These points of evidence suggest that a similar spatial disparity between FIR continuum as well as $H\alpha$ and OIR continuum may also exist in star-forming galaxies with infrared luminosity that is less than the SMGs. If true, the three-component dust model may be applicable to the massive star-forming galaxies at $z \sim 2$ in general.

5. Summary

In using data from ALMA and near-infrared IFUs, we study the 2D distributions of FIR continuum and $H\alpha$ for a sample of six $z \sim 2$ SMGs. The objectives are to study their relative distributions and sizes and to investigate the impact of the results on issues, such as the estimated SFRs, dust correction, dust distribution, and SED modeling. We summarize our findings as follows.

1. The sizes of $H\alpha$ are significantly ($>3\sigma$) larger than those of the FIR continuum in half of our sample of SMGs (Fig. 3). Across the sample, the $H\alpha$ sizes are a median factor of 2.0 ± 0.4 larger than the FIR sizes.
2. We find that the observed $H\alpha$ -based SFRs are systematically lower than the IR-based SFRs by a median factor of 20 ± 15 , and the factor is 4 ± 2 with the attenuation correction that applies the stellar A_V to $H\alpha$. By adopting the most extreme attenuation correction provided by Calzetti et al. (2000), the difference is still a factor of 3 ± 1 (Fig. 4).
3. By plotting the 1D SFR density profiles (Fig. 5), we find that less than 50% of the $H\alpha$ emissions come from outside the radii spanned by the dusty star-forming regions as traced by the FIR continuum. This is therefore not sufficient in explaining the differences found between $H\alpha$ -based SFRs and the IR-based SFRs. Given the expected high attenuation in the central dusty regions, we postulate that the majority of the obscured star formation is not reflected through the

extinction of OIR emissions, including $H\alpha$. This could be the case because in the scenario with the foreground screen of dust, the FIR continuum and OIR emissions are spatially decoupled due to extremely high A_V (>100). This could also be the result of the OIR emissions becoming optically thick due to high column density in the opposite scenario of dust mixing with stars. A combination of both scenarios is also possible.

4. To understand the impact of spatial mismatches on the energy balance SED modeling, we compare the A_V values derived from HYPERZ by using the OIR photometry alone and those from MAGPHYS. We find that the A_V values from MAGPHYS are significantly higher in two SMGs (one source is excluded due to foreground contaminations out of five), where the two have the highest IR luminosities among the sample. This suggests that the energy balance approach deduces a higher A_V to account for the extra IR luminosities. For the three SMGs in which the A_V values agree, we postulate that the contribution of the IR emissions from the birth clouds could be unrealistically high.
5. Finally, in considering the observed morphologies of $H\alpha$, OIR, and FIR continuum, together with our findings about SFRs and A_V , we postulate that the dust distributions in SMGs, and possibly also in less IR-luminous $z \sim 2$ star-forming galaxies, can be decomposed into the following three components: the diffuse ISM component obscuring the older stellar populations, the more obscured young star-forming H II regions, and the heavily obscured central regions with a low filling factor in which the bulk of attenuation cannot be reflected through $H\alpha$ or OIR continuum.

Future studies of a larger sample, in particular focusing on less IR luminous galaxies, would further improve our understandings of dust distribution and SFRs at $z \sim 2$.

Acknowledgements. We thank the anonymous referee for the constructive feedback that improved the manuscript. We also thank Richard Anderson for advices on the *Gaia* DR2 catalog. C.-C.C. is supported by an ESO fellowship program and is especially grateful to Tzu-Ying Lee (李姿瑩), who ensured the arrival of I-Fei Max Lee (李亦飛) during the time of this work. IRS and AMS acknowledge support from STFC (ST/P000541/1). JLW acknowledges support from an STFC Ernest Rutherford Fellowship (ST/P004784/2). MJM acknowledges the support of the National Science Centre, Poland, through the SONATA BIS grant 2018/30/E/ST9/00208. This paper makes use of the VLT data obtained through the following programs: 091.B-0920(E), 091.B-0920(C), 094.B-0798(B) and 096.A-0025(A). This paper also makes use of the following ALMA data: ADS/JAO.ALMA#2012.1.00307.S, ADS/JAO.ALMA#2015.1.01528.S, ADS/JAO.ALMA#2016.1.00434, and ADS/JAO.ALMA#2016.1.00735.S. ALMA is a partnership of ESO (representing its member states), NSF (USA) and NINS (Japan), together with NRC (Canada), MOST and ASIAA (Taiwan), and KASI (Republic of Korea), in cooperation with the Republic of Chile. The Joint ALMA Observatory is operated by ESO, AUI/NRAO and NAOJ. This research made use of Astropy (<http://www.astropy.org>) a community-developed core Python package for Astronomy (Astropy Collaboration 2013, 2018).

References

- Alaghband-Zadeh, S., Chapman, S. C., Swinbank, A. M., et al. 2012, *MNRAS*, **424**, 2232
- Apostolovski, Y., Aravena, M., Anguita, T., et al. 2019, *A&A*, **628**, A23
- Astropy Collaboration (Robitaille, T. P., et al.) 2013, *A&A*, **558**, A33
- Astropy Collaboration (Price-Whelan, A. M., et al.) 2018, *AJ*, **156**, 123
- Barger, A. J., Wang, W.-H., Cowie, L. L., et al. 2012, *ApJ*, **761**, 89
- Barro, G., Kriek, M., Pérez-González, P. G., et al. 2016, *ApJ*, **827**, L32
- Bendo, G. J., Boselli, A., Dariush, A., et al. 2012, *MNRAS*, **419**, 1833
- Biggs, A. D., & Ivison, R. J. 2008, *MNRAS*, **385**, 893
- Bolzonella, M., Miralles, J.-M., & Pelló, R. 2000, *A&A*, **363**, 476
- Bouwens, R. J., Illingworth, G. D., Oesch, P. A., et al. 2011, *ApJ*, **737**, 90
- Brammer, G. B., van Dokkum, P. G., & Coppi, P. 2008, *ApJ*, **686**, 1503
- Brown, M. J. I., Moustakas, J., Kennicutt, R. C., et al. 2017, *ApJ*, **847**, 136

- Bruzual, G., & Charlot, S. 2003, *MNRAS*, 344, 1000
- Calistro Rivera, G., Hodge, J. A., Smail, I., et al. 2018, *ApJ*, 863, 56
- Calzetti, D. 2013, in *Star Formation Rate Indicators*, eds. J. Falcon-Barroso, & J. H. Knapen, *Proceedings of the XXIII Canary Islands Winter School of Astrophysics: "Secular Evolution of Galaxies"*, 419
- Calzetti, D., Kinney, A. L., & Storch-Bergmann, T. 1994, *ApJ*, 429, 582
- Calzetti, D., Armus, L., Bohlin, R. C., et al. 2000, *ApJ*, 533, 682
- Calzetti, D., Kennicutt, R. C., Engelbracht, C. W., et al. 2007, *ApJ*, 666, 870
- Cardelli, J. A., Clayton, G. C., & Mathis, J. S. 1989, *ApJ*, 345, 245
- Carilli, C. L., Hodge, J., Walter, F., et al. 2011, *ApJ*, 739, L33
- Casey, C. M., Scoville, N. Z., Sanders, D. B., et al. 2014, *ApJ*, 796, 95
- Casey, C. M., Cooray, A., Killi, M., et al. 2017, *ApJ*, 840, 101
- Catalán-Torrecilla, C., Gil de Paz, A., Castillo-Morales, A., et al. 2015, *A&A*, 584, A87
- Chary, R., & Elbaz, D. 2001, *ApJ*, 556, 562
- Chen, C.-C., Smail, I., Swinbank, A. M., et al. 2015, *ApJ*, 799, 194
- Chen, C.-C., Smail, I., Swinbank, A. M., et al. 2016, *ApJ*, 831, 91
- Chen, C.-C., Hodge, J. A., Smail, I., et al. 2017, *ApJ*, 846, 108
- Cowie, L. L., Barger, A. J., Hsu, L.-Y., et al. 2017, *ApJ*, 837, 139
- Cowie, L. L., González-López, J., Barger, A. J., et al. 2018, *ApJ*, 865, 106
- da Cunha, E., Charlot, S., & Elbaz, D. 2008, *MNRAS*, 388, 1595
- da Cunha, E., Walter, F., Smail, I. R., et al. 2015, *ApJ*, 806, 110
- Danielson, A. L. R., Swinbank, A. M., Smail, I., et al. 2017, *ApJ*, 840, 78
- Davies, R. I. 2007, *MNRAS*, 375, 1099
- Davies, R. I., Agudo Berbel, A., Wierorrek, E., et al. 2013, *A&A*, 558, A56
- Dong, C., Spilker, J. S., Gonzalez, A. H., et al. 2019, *ApJ*, 873, 50
- Draine, B. T., Dale, D. A., Bendo, G., et al. 2007, *ApJ*, 663, 866
- Dunlop, J. S., McLure, R. J., Biggs, A. D., et al. 2017, *MNRAS*, 466, 861
- Elbaz, D., Dickinson, M., Hwang, H. S., et al. 2011, *A&A*, 533, A119
- Elbaz, D., Leiton, R., Nagar, N., et al. 2018, *A&A*, 616, A110
- Ellis, R. S., McLure, R. J., Dunlop, J. S., et al. 2013, *ApJ*, 763, L7
- Förster Schreiber, N. M., Renzini, A., Mancini, C., et al. 2018, *ApJS*, 238, 21
- Freudling, W., Romaniello, M., Bramich, D. M., et al. 2013, *A&A*, 559, A96
- Fujimoto, S., Ouchi, M., Shibuya, T., & Nagai, H. 2017, *ApJ*, 850, 83
- Fujimoto, S., Ouchi, M., Kohno, K., et al. 2018, *ApJ*, 861, 7
- Gaia Collaboration (Brown, A. G. A., et al.) 2018, *A&A*, 616, A1
- García-Marín, M., Colina, L., & Arribas, S. 2009, *A&A*, 505, 1017
- Geach, J. E., Dunlop, J. S., Halpern, M., et al. 2017, *MNRAS*, 465, 1789
- Ginolfi, M., Maiolino, R., Nagao, T., et al. 2017, *MNRAS*, 468, 3468
- Gómez-Guijarro, C., Toft, S., Karim, A., et al. 2018, *ApJ*, 856, 121
- Gruppioni, C., Pozzi, F., Rodighiero, G., et al. 2013, *MNRAS*, 432, 23
- Gullberg, B., Swinbank, A. M., Smail, I., et al. 2018, *ApJ*, 859, 12
- Hao, C.-N., Kennicutt, R. C., Johnson, B. D., et al. 2011, *ApJ*, 741, 124
- Harrison, C. M., Simpson, J. M., Stanley, F., et al. 2016, *MNRAS*, 457, L122
- Hickox, R. C., Wardlow, J. L., Smail, I., et al. 2012, *MNRAS*, 421, 284
- Ho, L. C., Feigelson, E. D., Townsley, L. K., et al. 2001, *ApJ*, 549, L51
- Hodge, J. A., Karim, A., Smail, I., et al. 2013, *ApJ*, 768, 91
- Hodge, J. A., Swinbank, A. M., Simpson, J. M., et al. 2016, *ApJ*, 833, 103
- Hodge, J. A., Smail, I., Walter, F., et al. 2019, *ApJ*, 876, 130
- Howell, J. H., Armus, L., Mazzarella, J. M., et al. 2010, *ApJ*, 715, 572
- Hsieh, B.-C., Wang, W.-H., Hsieh, C.-C., et al. 2012, *ApJS*, 203, 23
- Hurvich, C. M., & Tsai, C.-L. 1989, *Biometrika*, 76, 297
- Ikarashi, S., Ivison, R. J., Caputi, K. I., et al. 2015, *ApJ*, 810, 133
- Ikarashi, S., Caputi, K. I., Ohta, K., et al. 2017, *ApJ*, 849, L36
- Ishigaki, M., Kawamata, R., Ouchi, M., et al. 2018, *ApJ*, 854, 73
- Ivison, R. J., Swinbank, A. M., Swinyard, B., et al. 2010, *A&A*, 518, L35
- Karim, A., Swinbank, A. M., Hodge, J. A., et al. 2013, *MNRAS*, 432, 2
- Kashino, D., Silverman, J. D., Rodighiero, G., et al. 2013, *ApJ*, 777, L8
- Kennicutt, Jr., R. C. 1989, *ApJ*, 344, 685
- Kennicutt, R. C., & Evans, N. J. 2012, *ARA&A*, 50, 531
- Kennicutt, Jr., R. C., Hao, C.-N., Calzetti, D., et al. 2009, *ApJ*, 703, 1672
- Kocevski, D. D., Hasinger, G., Brightman, M., et al. 2018, *ApJS*, 236, 48
- Kreckel, K., Groves, B., Schinnerer, E., et al. 2013, *ApJ*, 771, 62
- Lawrence, A., Warren, S. J., Almaini, O., et al. 2007, *MNRAS*, 379, 1599
- Le Floc'h, E., Papovich, C., Dole, H., et al. 2005, *ApJ*, 632, 169
- Lehmer, B. D., Alexander, D. M., Bauer, F. E., et al. 2010, *ApJ*, 724, 559
- Leslie, S. K., Sargent, M. T., Schinnerer, E., et al. 2018, *A&A*, 615, A7
- Li, Y., Crocker, A. F., Calzetti, D., et al. 2013, *ApJ*, 768, 180
- Lilly, S. J., Eales, S. A., Gear, W. K. P., et al. 1999, *ApJ*, 518, 641
- Litke, K. C., Marrone, D. P., Spilker, J. S., et al. 2019, *ApJ*, 870, 80
- Liu, F. S., Jiang, D., Faber, S. M., et al. 2017, *ApJ*, 844, L2
- Luo, B., Brandt, W. N., Xue, Y. Q., et al. 2017, *ApJS*, 228, 2
- Madau, P., & Dickinson, M. 2014, *ARA&A*, 52, 415
- Martí-Vidal, I., Vlemmings, W. H. T., Muller, S., & Casey, S. 2014, *A&A*, 563, A136
- McLeod, D. J., McLure, R. J., & Dunlop, J. S. 2016, *MNRAS*, 459, 3812
- Menéndez-Delmestre, K., Blain, A. W., Swinbank, M., et al. 2013, *ApJ*, 767, 151
- Michałowski, M. J., Dunlop, J. S., Cirasuolo, M., et al. 2012, *A&A*, 541, A85
- Michałowski, M. J., Dunlop, J. S., Koprowski, M. P., et al. 2017, *MNRAS*, 469, 492
- Miettinen, O., Novak, M., Smolčić, V., et al. 2017, *A&A*, 602, A54
- Molina, J., Ibar, E., Swinbank, A. M., et al. 2017, *MNRAS*, 466, 892
- Murphy, E. J., Condon, J. J., Schinnerer, E., et al. 2011, *ApJ*, 737, 67
- Narayanan, D., Davé, R., Johnson, B. D., et al. 2018, *MNRAS*, 474, 1718
- Nelson, E. J., van Dokkum, P. G., Momcheva, I. G., et al. 2016, *ApJ*, 817, L9
- Nelson, E. J., Tadaki, K.-I., Tacconi, L. J., et al. 2019, *ApJ*, 870, 130
- Noeske, K. G., Faber, S. M., Weiner, B. J., et al. 2007, *ApJ*, 660, L47
- Noll, S., Burgarella, D., Giovannoli, E., et al. 2009, *A&A*, 507, 1793
- Oesch, P. A., Bouwens, R. J., Illingworth, G. D., et al. 2015, *ApJ*, 808, 104
- Oteo, I., Ivison, R. J., Negrello, M., et al. 2017, arXiv e-prints [arXiv:1709.04191]
- Peng, C. Y., Ho, L. C., Impy, C. D., & Rix, H.-W. 2010, *AJ*, 139, 2097
- Piqueras López, J., Colina, L., Arribas, S., & Alonso-Herrero, A. 2013, *A&A*, 553, A85
- Planck Collaboration XVI. 2014, *A&A*, 571, A16
- Popping, G., Puglisi, A., & Norman, C. A. 2017, *MNRAS*, 472, 2315
- Price, S. H., Kriek, M., Brammer, G. B., et al. 2014, *ApJ*, 788, 86
- Puglisi, A., Rodighiero, G., Franceschini, A., et al. 2016, *A&A*, 586, A83
- Ranalli, P., Comastri, A., & Setti, G. 2003, *A&A*, 399, 39
- Reddy, N. A., & Steidel, C. C. 2009, *ApJ*, 692, 778
- Reddy, N. A., Kriek, M., Shapley, A. E., et al. 2015, *ApJ*, 806, 259
- Rieke, G. H., Alonso-Herrero, A., Weiner, B. J., et al. 2009, *ApJ*, 692, 556
- Rousselot, P., Lidman, C., Cuby, J.-G., Moreels, G., & Monnet, G. 2000, *A&A*, 354, 1134
- Sanders, D. B., & Mirabel, I. F. 1996, *ARA&A*, 34, 749
- Schmidt, M. 1959, *ApJ*, 129, 243
- Scholtz, J., Alexander, D. M., Harrison, C. M., et al. 2018, *MNRAS*, 475, 1288
- Scholtz, J., Harrison, C. M., Rosario, D. J., et al. 2020, *MNRAS*, 492, 3194
- Schreiber, C., Pannella, M., Elbaz, D., et al. 2015, *A&A*, 575, A74
- Shivaei, I., Kriek, M., Reddy, N. A., et al. 2016, *ApJ*, 820, L23
- Simpson, J. M., Swinbank, A. M., Smail, I., et al. 2014, *ApJ*, 788, 125
- Simpson, J. M., Smail, I., Swinbank, A. M., et al. 2015, *ApJ*, 799, 81
- Simpson, J. M., Smail, I., Swinbank, A. M., et al. 2017, *ApJ*, 839, 58
- Siringo, G., Kreysa, E., Kovács, A., et al. 2009, *A&A*, 497, 945
- Smolčić, V., Schinnerer, E., Zamorani, G., et al. 2009, *ApJ*, 690, 610
- Sobral, D., Smail, I., Best, P. N., et al. 2013, *MNRAS*, 428, 1128
- Somerville, R. S., & Davé, R. 2015, *ARA&A*, 53, 51
- Spilker, J. S., Aravena, M., Marrone, D. P., et al. 2015, *ApJ*, 811, 124
- Spilker, J. S., Marrone, D. P., Aravena, M., et al. 2016, *ApJ*, 826, 112
- Stach, S. M., Smail, I., Swinbank, A. M., et al. 2018, *ApJ*, 860, 161
- Stach, S. M., Dudzeviciute, U., Smail, I., et al. 2019, *MNRAS*, 487, 4648
- Stanley, F., Harrison, C. M., Alexander, D. M., et al. 2018, *MNRAS*, 478, 3721
- Swinbank, A. M., Smail, I., Chapman, S. C., et al. 2004, *ApJ*, 617, 64
- Swinbank, A. M., Chapman, S. C., Smail, I., et al. 2006, *MNRAS*, 371, 465
- Swinbank, A. M., Simpson, J. M., Smail, I., et al. 2014, *MNRAS*, 438, 1267
- Tadaki, K.-I., Genzel, R., Kodama, T., et al. 2017a, *ApJ*, 834, 135
- Tadaki, K.-I., Kodama, T., Nelson, E. J., et al. 2017b, *ApJ*, 841, L25
- Takata, T., Sekiguchi, K., Smail, I., et al. 2006, *ApJ*, 651, 713
- Taylor, E. N., Franx, M., van Dokkum, P. G., et al. 2009, *ApJS*, 183, 295
- Theios, R. L., Steidel, C. C., Strom, A. L., et al. 2019, *ApJ*, 871, 128
- Thomson, A. P., Smail, I., Swinbank, A. M., et al. 2019, *ApJ*, 883, 204
- Toft, S., Smolčić, V., Magnelli, B., et al. 2014, *ApJ*, 782, 68
- Turner, O. J., Cirasuolo, M., Harrison, C. M., et al. 2017, *MNRAS*, 471, 1280
- van der Wel, A., Franx, M., van Dokkum, P. G., et al. 2014, *ApJ*, 788, 28
- Wardlow, J. L., Smail, I., Coppin, K. E. K., et al. 2011, *MNRAS*, 415, 1479
- Weiß, A., Kovács, A., Coppin, K., et al. 2009, *ApJ*, 707, 1201
- Whitaker, K. E., van Dokkum, P. G., Brammer, G., & Franx, M. 2012, *ApJ*, 754, L29
- Wild, V., Charlot, S., Brinchmann, J., et al. 2011, *MNRAS*, 417, 1760
- Wilkinson, A., Almaini, O., Chen, C.-C., et al. 2017, *MNRAS*, 464, 1380
- Wisnioski, E., Förster Schreiber, N. M., Wuyts, S., et al. 2015, *ApJ*, 799, 209
- Wuyts, S., Förster Schreiber, N. M., Genzel, R., et al. 2012, *ApJ*, 753, 114
- Wuyts, S., Förster Schreiber, N. M., Nelson, E. J., et al. 2013, *ApJ*, 779, 135
- Xue, Y. Q., Luo, B., Brandt, W. N., et al. 2011, *ApJS*, 195, 10